



Acute pharmacological inhibition of matrix metalloproteinase-9 activity during development restores perineuronal net formation and normalizes auditory processing in *Fmr1* KO mice

Patricia S. Pirbhoy¹ | Maham Rais¹ | Jonathan W. Lovelace² | Walker Woodard¹ | Khaleel A. Razak² | Devin K. Binder¹ | Iryna M. Ethell¹

¹Division of Biomedical Sciences, School of Medicine, University of California, Riverside, CA, USA

²Department of Psychology, University of California Riverside, Riverside, CA, USA

Correspondence

Iryna M. Ethell, Division of Biomedical Sciences, School of Medicine, University of California, Riverside, Riverside, CA 92521, USA.

Email: iryna.ethell@medsch.ucr.edu

Funding information

National Institute of Mental Health, National Institute of Child Health and Human Development, Grant/Award Number: U54 HD082008-01; National Institute of Mental Health; National Institute of Child Health and Human Development; FRAXA Research Foundation, Grant/Award Number: Postdoctoral Fellowship ; University of California President's Postdoctoral Fellowship Program

Abstract

Individuals with Fragile X Syndrome (FXS) and autism spectrum disorder (ASD) exhibit cognitive impairments, social deficits, increased anxiety, and sensory hyperexcitability. Previously, we showed that elevated levels of matrix metalloproteinase-9 (MMP-9) may contribute to abnormal development of parvalbumin (PV) interneurons and perineuronal nets (PNNs) in the developing auditory cortex (AC) of *Fmr1* knock-out (KO) mice, which likely underlie auditory hypersensitivity. Thus, MMP-9 may serve as a potential target for treatment of auditory hypersensitivity in FXS. Here, we used the MMP-2/9 inhibitor, SB-3CT, to pharmacologically inhibit MMP-9 activity during a specific developmental period and to test whether inhibition of MMP-9 activity reverses neural oscillation deficits and behavioral impairments by enhancing PNN formation around PV cells in *Fmr1* KO mice. Electroencephalography (EEG) was used to measure resting state and sound-evoked electrocortical activity in auditory and frontal cortices of postnatal day (P)22–23 male mice before and one-day after treatment with SB-3CT (25 mg/kg) or vehicle. At P27–28, animal behaviors were tested to measure the effects of the treatment on anxiety and hyperactivity. Results show that acute inhibition of MMP-9 activity improved evoked synchronization to auditory stimuli and ameliorated mouse behavioral deficits. MMP-9 inhibition enhanced PNN formation, increased PV levels and TrkB phosphorylation yet reduced Akt phosphorylation in the AC of *Fmr1* KO mice. Our results show that MMP-9 inhibition during early postnatal development is beneficial in reducing some auditory processing deficits in the FXS mouse model and may serve as a candidate therapeutic for reversing sensory hypersensitivity in FXS and possibly other ASDs.

KEYWORDS

electroencephalography, fragile X syndrome, matrix metalloproteinase-9, parvalbumin, perineuronal nets, sensory hypersensitivity

Abbreviations: AC, auditory cortex; Akt, protein kinase B; ASD, autism spectrum disorders; EEG, electroencephalography; FC, frontal cortex; FFT, fast fourier transform; *Fmr1* KO, *Fragile X mental retardation 1* gene knock-out; FXS, fragile X syndrome; ITPC, inter-trial phase coherence; MMP-2/9, matrix metalloproteinase-2/9; mTOR, mammalian target of rapamycin; PNN, perineuronal net; PV, parvalbumin; RRID, research resource identifier; STP, single trial power; TrkB, tropomyosin-related kinase B.

1 | INTRODUCTION

Fragile X Syndrome (FXS) is a neurodevelopmental disorder caused by the hypermethylation of the *Fragile X mental retardation 1 (Fmr1)* gene, resulting in the loss of the Fragile X Mental Retardation Protein (FMRP) (Verkerk et al., 1991), a regulator of protein synthesis (Laggerbauer, 2001). FXS is the most prevalent cause of inherited intellectual disability (Hagerman, Rivera, & Hagerman, 2008) and a leading genetic cause of autism, providing a genetic model to study the neurobiological mechanisms underlying autism spectrum disorders (ASD) (Crawford, Acuna, & Sherman, 2001; Hagerman et al., 2008). Individuals with FXS exhibit cognitive dysfunctions (Freund & Reiss 1991; Kaufmann et al., 2004), increased anxiety (Talisa, Boyle, Crafa, & Kaufmann, 2014), and sensory hyperexcitability (Ethridge et al., 2016; Miller et al., 1999; Rotschafer & Razak, 2013).

Auditory hypersensitivity in individuals with FXS and *Fmr1* knock-out (KO) mice is commonly characterized by a heightened response to non-aversive stimuli (Crane, Goddard, & Pring, 2009; McDiarmid, Bernardos, & Rankin, 2017; Rais, Binder, Razak, & Ethell, 2018; Sinclair, Oranje, Razak, Siegel, & Schmid, 2017), reduced ability to habituate to sounds (Castren, Paakkonen, Tarkka, Ryyanen, & Partanen, 2003; Ethridge et al., 2016; Lovelace et al., 2016; Wang et al., 2017), and greater resting state gamma power in electroencephalography (EEG) recordings (Ethridge et al., 2017; Lovelace, Ethell, Binder, & Razak, 2018; Lovelace et al., 2019; Wang et al., 2017). Studies in the *Fmr1* KO mice also show increased sensory responses, broader receptive fields, impaired sound selectivity (Rotschafer & Razak, 2013), and abnormal network synchronization (Paluszkiwicz, Olmos-Serrano, Corbin, & Huntsman, 2011). It is hypothesized that the inability to habituate to auditory stimuli (Castren et al., 2003; Ethridge et al., 2016) including ongoing background noise, a phenotype that is also observed in *Fmr1* KO mice (Lovelace et al., 2016, 2018), may contribute to hypersensitivity to sounds and cortical hyperexcitability (Ethridge et al., 2016, 2017; Gibson, Bartley, Hays, & Huber, 2008; Lovelace et al., 2018, 2019). Notably, EEG gamma frequency band abnormalities are associated with heightened sensory sensitivities and social communication deficits in FXS individuals (Ethridge et al., 2016, 2017, 2019). Taking advantage of the link between EEG abnormalities and sensory hypersensitivity in FXS, this study used these EEG measures to test the efficacy of a candidate treatment in *Fmr1* KO mice.

Individuals with FXS (Dziembowska et al., 2013) and *Fmr1* KO mice (Bilousova et al., 2009; Gkogkas et al., 2014; Sidhu, Dansie, Hickmott, Ethell, & Ethell, 2014) exhibit increased levels of the secreted endopeptidase, matrix metalloproteinase-9 (MMP-9). Specifically, *Fmr1* KO mice show elevated levels of MMP-9 in the auditory cortex (AC) during postnatal day (P) 3–18 period. It is hypothesized that increased activity of MMP-9 may contribute to the development of auditory hypersensitivity by excessively degrading PNNs, thereby resulting in impaired PNN formation around PV interneurons and affecting PV development in the AC of *Fmr1* KO mice at P21 (Wen et al., 2018). Indeed, genetic reduction of MMP-9

levels enhanced PNN formation around PV interneurons and restored sound-evoked responses and spontaneous activity to WT levels (Wen et al., 2018). Genetic removal of MMP-9 also rescued altered event-related potential (ERP) habituation responses in the AC of adult *Fmr1* KO mice (Lovelace et al., 2016), normalized dendritic spine abnormalities in the hippocampus and improved abnormal behaviors in *Fmr1* KO mice (Sidhu et al., 2014). PV interneuron dysfunction contributes to abnormal network synchrony and alterations in gamma oscillations (Lewis, Hashimoto, & Volk, 2005; Sohal, Zhang, Yizhar, & Deisseroth, 2009; Vreugdenhil, Jefferys, Celio, & Schwaller, 2003). Overall, these studies indicate that (1) MMP-9 may influence the development of hypersensitive networks during the third and fourth postnatal weeks, a time that coincides with a critical developmental window for inhibitory and excitatory circuit maturation (Gibson et al., 2008; Oswald & Reyes, 2008) and (2) that targeted inhibition of MMP-9 may serve as a candidate therapeutic to reduce auditory hypersensitivity in FXS.

In this study, we tested the hypothesis that acute pharmacological inhibition of aberrant MMP-9 activity during the critical developmental period would ameliorate cortical processing deficits, including abnormal resting state neural oscillatory patterns, the ability to synchronize to stimulus-induced oscillations, PV/PNN deficits, and behavioral impairments. Our results show that acute inhibition of MMP-9 during the P22–23 developmental period improved evoked synchronization to auditory stimuli and enhanced PNN formation around PV cells. We also observed beneficial effects of acute MMP-9 inhibition at P27–28 on animal behaviors, such as anxiety and hyperactivity. MMP-9 inhibition at P27–28 also increased PV levels and TrkB phosphorylation, and reduced aberrant Akt phosphorylation in the developing AC of *Fmr1* KO mice.

2 | MATERIALS AND METHODS

2.1 | Ethics statement

All experiments and animal care/use protocols were approved by the Institutional Animal Care and Use Committee at the University of California, Riverside (approval number 20190015 and 20190029) and were carried out in accordance with NIH 'Guide for the Care and Use of Laboratory Animals'. The study was not pre-registered.

2.2 | Animals

Experimental animals, C57BL/6 mice, were obtained from Jackson Laboratories (RRID: IMSR_JAX:003025). Age-matched wild-type (WT) and *Fmr1* KO male mice were used between postnatal day (P) 18–19 (EEG surgery $N = 79$, $N = 14$ died post-surgery), P22–23 (EEG recording [$N = 65$] and PV/PNN analysis [$N = 24$: note the same EEG animals were used for analysis] and DQ gelatin assay [$N = 16$]), and P27–29 for behavior ($N = 37$) and Western blot ($N = 8$). For a detailed description of total animals and animals per group, please

refer to Figures 1, 6, and 7. A total of 140 male mice were used in this study with an average weight of 8 g and range from 6 to 18 g. All genotypes were confirmed with the analysis of tail samples by Transnetyx, using real-time PCR-based system to probe for WT (*fmr*^{+/+}-forward: 5'-TGTGATAGAATATGCAGCATGTGA-3') or KO (*fmr*^{-/-}-forward: 5'CACGAGACTAGTGAGACGTG-3') target sequence in each sample. Mice were maintained in an AAALAC accredited facility in 12-hr light/dark cycles and food and water was available ad libitum. All experimental procedures were performed on C57BL/6 (WT, RRID:IMSR_JAX:000664) and *Fragile X mental retardation gene-1* (*Fmr1*) knock-out (KO) mice (RRID: IMSR_JAX:003025, The Jackson Laboratory).

2.3 | Surgery for electroencephalography recordings

Surgical procedures were performed as described in detail previously (Lovelace et al., 2018, 2019). Briefly, mice were anesthetized with isoflurane inhalation (0.2%–0.5%) and given an intraperitoneal (i.p.) injection of ketamine and xylazine (K/X: 100/20 mg/kg). Toe pinch reflex was used to measure anesthetic state every 10 min throughout the surgery, and supplemental doses, no more than half of the original dose of K/X, were administered as needed. Mice were placed in a stereotaxic frame (model 930; Kopf, CA). Artificial tear gel was applied to the eyes to prevent drying. Once the mouse was anesthetized, a midline sagittal incision was made along the scalp to expose the skull. A Foredom dental drill was used to drill three holes 1 mm in diameter in the skull overlying the right AC (−1.6 mm, +4.8 mm), right frontal lobe (+2.6 mm, +1.0 mm), and left occipital cortex (−3.5 mm, −5.2 mm) (coordinate relative to bregma: anterior/posterior, medial/lateral). Three channel electrode posts (Plastics One, MS333-2-A-SPC) were attached to 1-mm stainless steel screws (Plastics One, 8L003905201F) and screws were advanced into the drilled holes until secure. Special care was taken not to advance the screws beyond the point of contact with the dura. Dental cement was applied around the screws, on the base of the post, and exposed skull. Postoperative care included topical application of a triple antibiotic ointment along the edges of the dental cement followed by two subcutaneous injections of buprenorphine (0.05 mg/kg), one immediately after surgery, and one 6–10 hr after surgery. Mice were placed on a heating pad to aid recovery from anesthesia. Mice were group housed, returned to the vivarium, and monitored daily until the day of EEG recordings, which allowed 4–5 days recovery post-surgery before recording.

2.4 | Electrophysiology

All EEG recordings were performed during 5 a.m.–7 p.m. Mice were habituated for 20 min in an anechoic foam-lined sound-attenuating chamber (Gretch-Ken Industries Inc.) and connected to the BioPac acquisition system (BIOPAC Systems, Inc) through a three-channel tether under brief isoflurane anesthesia. The tether was connected

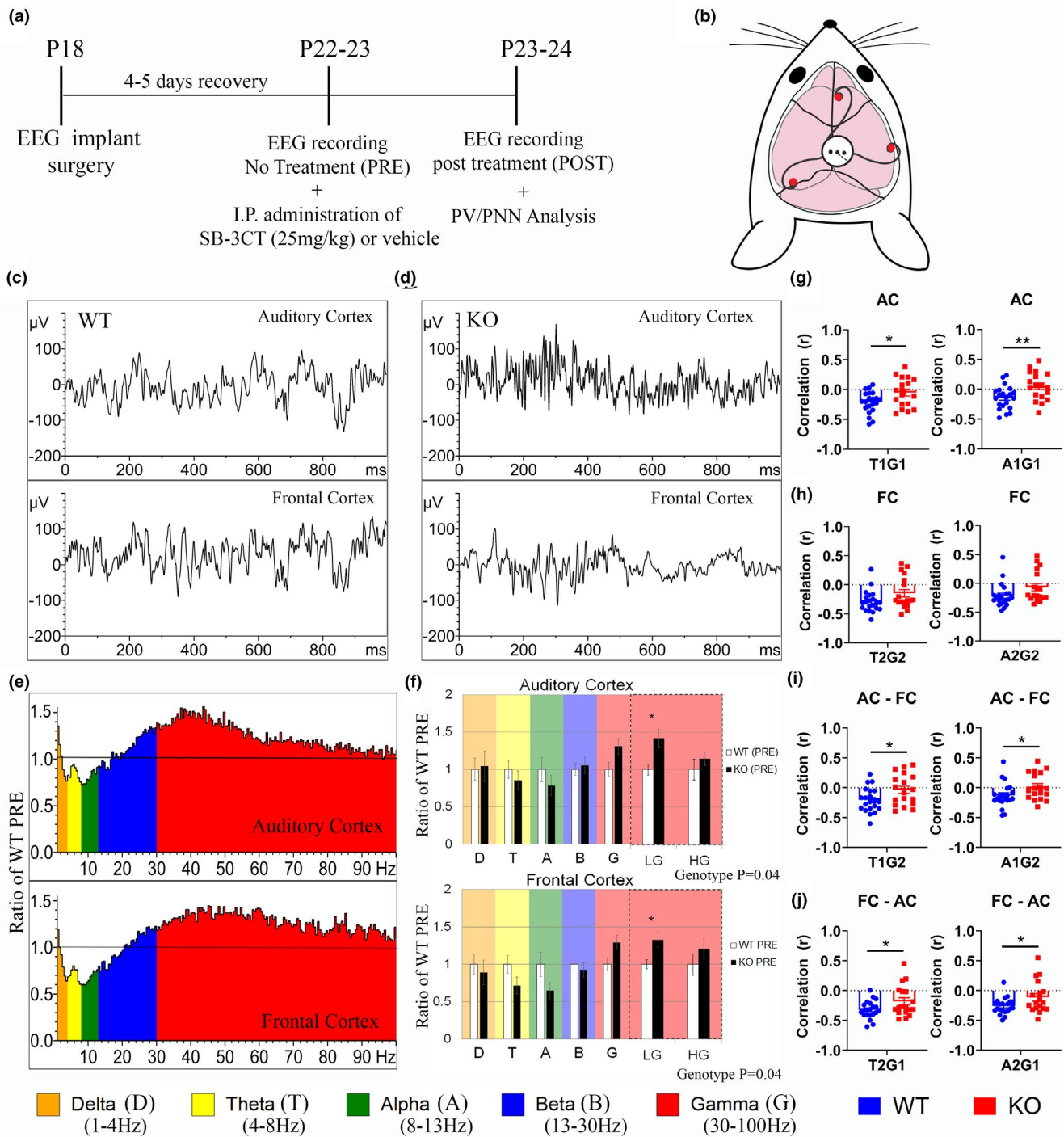
to a commutator located directly above the cage. Mice were then allowed to habituate to being connected to the tether for an additional 15 min before EEG recordings were obtained. During the recording session, a piezoelectric sensor placed under the floor of the cage detected mouse movement in the recording arena.

EEG activity was obtained using the BioPac system and Acqknowledge recording software from awake and freely moving mice. The BioPac MP150 acquisition system was connected to two EEG 100C amplifier units (one for each channel) to which the commutator was attached. The lead to the occipital cortex served as a reference for both frontal and auditory cortex screw electrodes. The acquisition hardware was set to high-pass (> 0.5 Hz) and low-pass (< 100 Hz) filters. Normal EEG output data were collected with gain maintained the same (10,000 X) between all recordings. Data were sampled at a rate of 2.5 kHz using Acqknowledge software and down sampled to 1,024 Hz post hoc using Analyzer 2.1 (Brain Vision LLC). Sound delivery was synchronized with EEG recording using a TTL pulse to mark the onset of each sound in a train. Resting EEGs were recorded for 5 min (during this time no auditory stimuli were presented) followed by recordings in response to auditory stimulation. After all EEG experiments were completed, mice were perfused for histology or used for behavioral tasks and Western blot analysis.

2.5 | Acoustic stimulation

Acoustic stimulation paradigms were similar as those previously used in *Fmr1* KO mice (Lovelace et al., 2018, 2019), which is analogous to work in humans with FXS. Acoustic stimuli were generated using RPvdsEx software and RZ6 hardware (Tucker-Davis Technologies) and presented through a free-field speaker (MF1 Multi-Field Magnetic Speaker; Tucker-Davis Technologies) located 30 cm away directly above the cage. Sound pressure level (SPL) was modified using programmable attenuators in the RZ6 system. The speaker output was ~ 70 dB SPL at the floor of recording chamber with fluctuation of ± 3 dB for frequencies between 5 and 35 kHz as measured with a ¼ in Bruel and Kjaer microphone.

A chirp-modulated signal (henceforth 'chirp') to induce synchronized oscillations in EEG recordings was used to quantify fidelity of responses to time-varying stimuli. The chirp is a two-second broadband noise stimulus with amplitude modulated (100% modulation depth) by a sinusoid whose frequencies increase (Up-chirp) or decrease (Down-chirp) linearly in the 1–100 Hz range (Artieda et al., 2004; Perez-Alcazar et al., 2008; Purcell, John, Schneider, & Picton, 2004). The chirp facilitates a rapid measurement of transient oscillatory response (delta to gamma frequency range) to auditory stimuli of varying frequencies and can be used to compare oscillatory response in different groups in clinical and preclinical settings. Inter-trial phase coherence analysis (phase locking factor) can then be used to determine the ability of the neural generator to synchronize oscillations to the frequencies present in the stimulus (Tallon-Baudry, Bertrand, Delpuech, & Pernier, 1996). The chirp stimulus may be preferable over the traditional steady state stimulus



in studies of children with neurodevelopmental disorders, as it can quickly and efficiently measure multiple modulation frequencies in a shorter period of time.

To avoid onset responses contaminating phase locking to the amplitude modulation of the chirp, the stimulus was ramped in sound level from 0% to 100% over 1 s (rise time), which then smoothly transitioned into chirp modulation of the noise (see Figure 3c for example). Up- and Down-chirp trains were presented 300 times each (for a total of 600 trains). Both directions of modulation were tested to ensure any frequency-specific effects were

not due to the frequency transition history within the stimulus. Up- and Down-chirp trains were presented in an alternating sequence. The interval between each train was randomly varied between 1 and 1.5 s.

2.6 | Data analysis

All EEG data analyses were performed as described previously (Lovelace et al., 2018, 2019). Briefly, EEG data were extracted from

FIGURE 1 Developing *Fmr1* KO mice exhibit increased low gamma power. (a) Experimental timeline shows mice were implanted at P18 with two-channel EEG electrodes (WT, $N = 35$; *Fmr1* KO, $N = 30$) in the auditory cortex (AC) and the frontal cortex (FC), and with an occipital cortex reference electrode. Animals were allowed 4–5 days to recover post-surgery (WT, $N = 35$; *Fmr1* KO, $N = 30$; $N = 14$ (WT $N = 8$; KO $N = 6$) animals died post-surgery) and EEG recording was done prior to treatment (PRE) at P22–23 (WT, $N = 23$, excluded $N = 1$; *Fmr1* KO, $N = 21$, excluded $N = 1$). Immediately after the EEG recording, animals were given either an intraperitoneal injection of SB-3CT (25 mg/kg) or vehicle. At P23–24, a post-treatment EEG recording was performed. Brains were collected for PV/PNN analysis immediately after EEG recording. (b) Schematic shows placement of electrodes, which consisted of a three-channel electrode post with three 1-mm stainless steel screws (depicted by red dots). (c–j) EEG recording was done prior to treatment (PRE) at P22–23. Resting data (baseline, in the absence of auditory stimulation) were collected for 5 min and divided into 2-s segments for spectral analysis. Depicted are examples of EEG segments from individual WT (c) and *Fmr1* KO (d) mice, which include simultaneous recording from the AC and the FC. (e and f) Graphs show average spectral power ($\mu\text{V}^2/\text{Hz}$) in the AC and FC of *Fmr1* KO mice ($N = 20$) in a histogram (e) and bar graph format (f) expressed as the ratio of WT controls ($N = 22$) prior to treatment (PRE). A value of 1 indicates no mean difference in power between WT and *Fmr1* KO mice, while values above the black line indicate KO > WT, and below indicate KO < WT. (f) Statistical analysis was performed using a one-way MANCOVA with the percentage of time spent moving as a covariate. Genotype differences were compared using six spectral bands per region: Delta (D), Theta (T), Alpha (A), Beta (B), Low Gamma (LG), and High Gamma (HG). Since assumptions were not violated, we report an effect of genotype (AC: Pillai's Trace = 2.465, $p = .04$; FC: Pillai's Trace = 2.587, $p = .036$) across all six of the combined frequency variables. Low gamma was significantly increased after correction for multiple comparisons in the both the AC and FC: AC low gamma, $F(1,27) = 10$, $p = .003$, $\eta^2 = 0.204$, FC low gamma, $F(1,27) = 9.012$, $p = .005$, $\eta^2 = 0.188$ (WT $N = 22$, *Fmr1* KO $N = 20$). All graphs represent average values and the error bars indicate SEM. To determine whether there is a relationship between power across different frequencies and/or regions, a Pearson's correlation was done for resting baseline segments comparing *Fmr1* KO ($N = 21$, excluded $N = 3$) versus WT control mice ($N = 23$, excluded $N = 2$). (g) Graph shows Pearson's correlation (r) for each mouse for AC Theta/Low Gamma and AC Alpha/Low Gamma (WT, $N = 21$; *Fmr1* KO, $N = 18$; T1G1: $p = .02$; A1G1: $p = .008$). (h) Graph shows the Pearson's correlation (r) for FC Theta/Low Gamma and FC Alpha/Low Gamma. (i) Graph shows the Pearson's correlation (r) for AC Theta/FC Low Gamma and AC Alpha/FC Low Gamma (T1G2: $p = .03$; A1G2: $p = .04$). (j) Graph shows the Pearson's correlation (r) for the FC Theta/AC Low Gamma and FC Alpha/AC Low Gamma (T2G1: $p = .04$; A2G1: $p = .03$). For power coupling comparisons, animals that moved < 5% during the resting baseline were excluded from the analysis

Acqknowledge and converted to files compatible with Analyzer 2.1 software. All data were notched filtered at 60 Hz to remove residual line noise from recordings. Artifact rejection was performed using BrainVision Analyzer. Several criteria were used to search for artifacts including amplitude, gradient, max-min, and low activity. Less than 30% of data were rejected due to artifacts from any single mouse. If more than 30% of the data was rejected, the animal was excluded from analysis (Resting baseline: WT PRE, $N = 1$; *Fmr1* KO PRE, $N = 1$; vehicle-treated *Fmr1* KO, $N = 2$; vehicle-treated WT, $N = 2$; SB-3CT-treated *Fmr1* KO, $N = 1$; Chirp: *Fmr1* KO PRE, $N = 2$, vehicle-treated WT, $N = 1$; SB-3CT-treated WT, $N = 1$; *Fmr1* KO, $N = 2$, SB-3CT-treated *Fmr1* KO, $N = 1$). Notably, no outlier test was performed; instead, animals were excluded based on the exclusion criterion described above or movement percentage.

2.7 | Resting EEG analysis

Five minutes of EEG data (no auditory stimulus) were divided into 2-s segments and Fast Fourier Transforms (FFT) were calculated on each segment using 0.5 Hz bins, using a Hanning window, with no overlap, and then average power ($\mu\text{V}^2/\text{Hz}$) was calculated for each mouse from 1 to 100 Hz. Power was then further binned into standard frequency bands. We compared genotype mean differences on six bands per region: Delta (1–4 Hz), Theta (4–8 Hz), Alpha (8–13 Hz), Beta (13–30 Hz), Low Gamma (30–55 Hz), and High Gamma (65–100 Hz). The gamma band (30–100 Hz) was divided into low (30–60 Hz) versus high (> 60 Hz) bands in gamma range because studies show that the lower gamma frequency rhythm may be associated with activity of PV cells (Balakrishnan & Pearce, 2014; Dvorak &

Fenton, 2014; Ray & Maunsell, 2011), whereas the higher gamma frequencies may be related to spiking activity near the electrodes (Buzsaki & Wang, 2012; Ray & Maunsell, 2011). The spectral bands used are based on a number of previous studies on FXS in both mice (Radwan, Dvorak, & Fenton, 2016) and humans (Ethridge et al., 2016, 2017; Wang et al., 2017).

Responses to chirp trains were analyzed using Morlet wavelet analysis. Chirp trains were segmented into windows of 500 ms before chirp onset to 500 ms after the end of the chirp sound (total of 3 s because each chirp was 2 s in duration). EEG traces were processed with Morlet wavelets from 1 to 100 Hz using complex number output (voltage density, $\mu\text{V}/\text{Hz}$) for Inter-Trial Phase Coherence (ITPC) calculations, and power density ($\mu\text{V}^2/\text{Hz}$) for non-phase locked single trial power (STP). Wavelets were run with a Morlet parameter of 10 as this gave the best frequency/power discrimination. This parameter was chosen since studies in humans found most robust difference around 40 Hz, where this parameter is centered (Ethridge et al., 2017). To measure phase synchronization at each frequency across trials, Inter-Trial Phase Coherence (ITPC) was calculated. The equation used to calculate ITPC is as follows:

$$ITPC(f,t) = \frac{1}{n} \sum_{k=1}^n \frac{F_k(f,t)}{|F_k(f,t)|}$$

where f is the frequency, t is the time point, and k is the trial number. Thus, $F_k(f,t)$ refers to the complex wavelet coefficient at a given frequency and time for the k th trial. There were no < 225 trials (out of 300) for any given mouse after segments containing artifacts were rejected.

2.8 | Statistical analysis and definition of movement states

All statistical analysis was performed as described previously (Lovelace et al., 2018, 2019). Statistical group comparisons of chirp responses (ITPC and STP) were quantified by wavelet analysis using MATLAB (MATLAB, RRID:SCR_001622). The analysis was conducted by binning time (2 s segments) into 256 parts and frequency into 100 parts, resulting in a 100×256 matrix. Non-parametric cluster analysis was used to determine contiguous regions in the matrix that were significantly different from a distribution of 2000 randomized Monte Carlo permutations based on previously published methods (Maris & Oostenveld, 2007). Briefly, if the cluster size of the real genotype assignments (both positive and negative direction, resulting in a two-tailed alpha of $p = .025$) were larger than 97.25% of the random group assignments, those clusters were considered significantly different between genotypes. This method avoids statistical assumptions about the data and corrects for multiple comparisons. In all cases, $p < .05$ was considered significant for ANOVA and Student's *t* tests. Where *t* tests were performed, *r* was calculated as an effect size. When interactions were found and multiple comparisons for ANOVA were made, data were analyzed on each factor for simple effects and corrected using Bonferroni adjustments. If assumptions of sphericity were violated for repeated measures ANOVA, the Greenhouse–Geisser correction was used.

As movement can alter cortical gain (Niell & Stryker, 2010), and *Fmr1* KO mice show hyperactivity, a piezoelectric transducer was placed under the EEG recording arena to detect when the mouse was moving. The term 'resting' is used to indicate EEGs recorded in these mice without any specific auditory stimuli. The term 'still' is used to describe resting EEG when the mouse was stationary. The term 'moving' is used to describe resting EEG when the mouse was moving based on a threshold criterion for the piezoelectric signal that was confirmed by analyzing the video recording (under IR light) that was taken throughout the EEG recording procedure. In all cases where genotype means are reported, standard error of the mean (SEM) was used. The genotype differences in resting power were analyzed on six dependent variables using one-way Multivariate analysis of co-variance (MANCOVA) with one covariate (movement), independent variables (IV): genotype (*Fmr1* KO, WT), dependent variables (DV): six frequency bins (delta to high gamma). The proportion of time spent moving during the 5-min recording session was used as a covariate to isolate effects of genotype and control for the effect movement has on cortical gain. When multiple comparisons for MANCOVA were made, genotype comparisons were corrected using Bonferroni adjustments. The divisor for Bonferroni correction for multiple comparisons (for six frequency bands) on MANCOVA was set to 6, $\alpha = 0.05/6 = 0.0083$. Data are often expressed and plotted as ratio of control group values to gauge relative differences in various factors using the same scale. Statistical analysis was done using SPSS software package (SPSS, RRID:SCR_002865).

2.9 | Treatment

The matrix metalloproteinase-2/9 inhibitor, SB-3CT, in saline containing 10% DMSO (Millipore, Cat. 444274), or vehicle (10% DMSO in saline) was administered intraperitoneally (i.p., 25 mg/kg) to WT and *Fmr1* KO mice at P22–23 (for timeline, see Figure 1a). For treatment, animals were assigned based on simple randomization. To blind experimenter to treatment, animals were given a numerical identifier with no treatment identification that was used during EEG recording and PV/PNN analysis. A second group of mice that did not undergo EEG surgery or recording received a single treatment of SB-3CT (25 mg/kg) or vehicle injections at P27–28 and were subjected to behavioral tests at P28–29 (Figure 6a). To blind experimenter to treatments during behavior, tests were performed by two experimenters, one experimenter administered treatment and second experimenter was blinded to assigned treatment of each mouse. A third group that did not undergo EEG surgery or recording received a single treatment of SB-3CT (25 mg/kg) or vehicle injections at P21–22 (Figure 7a). To blind experimenter to treatments, one experimenter prepared drugs and assigned a numerical identifier to each treatment/animal and a second experimenter administered the treatment and was blinded to each assigned treatment. Initial number of animals used per group: EEG implant surgery (WT, $N = 35$; *Fmr1* KO, $N = 30$), EEG recording (WT PRE, $N = 23$; *Fmr1* KO PRE, $N = 21$; vehicle-treated WT, $N = 18$; SB-3CT-treated WT, $N = 15$; vehicle-treated *Fmr1* KO, $N = 14$; SB-3CT-treated *Fmr1* KO, $N = 13$), PV/PNN analysis ($N = 6$ per group; vehicle-treated WT, $n = 18$; SB-3CT-treated WT, $n = 23$; vehicle-treated *Fmr1* KO, $n = 20$; SB-3CT-treated *Fmr1* KO, $n = 17$), behavior (vehicle-treated *Fmr1* KO, $N = 10$; SB-3CT-treated *Fmr1* KO, $N = 9$; vehicle-treated WT, $N = 10$; SB-3CT-treated WT, $N = 8$), Western blot (vehicle-treated *Fmr1* KO, $N = 4$; SB-3CT-treated *Fmr1* KO, $N = 4$; vehicle-treated WT, $N = 4$; SB-3CT-treated WT, $N = 4$), and DQ gelatin assay (vehicle-treated *Fmr1* KO, $N = 5$; SB-3CT-treated *Fmr1* KO, $N = 5$; vehicle-treated WT, $N = 3$; SB-3CT-treated WT, $N = 3$).

2.10 | Dye-quenched (DQ) gelatin assay and analysis

The dye-quenched (DQ) gelatinase activity assay is a hydrolytic activity assay used to measure MMP-2/9 activity. The DQ gelatin assay measures MMP-2/9 activity by measuring the fluorescent intensity of a FITC-quenched gelatin peptide that fluoresces following cleavage by MMP-2 or MMP-9 to measure MMP-2/MMP-9 proteolytic activity (Vandooren et al., 2011). To confirm that i.p. administration of SB-3CT results in the inhibition of MMP-9 activity in the brain, 1 hr after treatment with SB-3CT inhibitor or vehicle P22 WT mice ($N = 3$ per group) were euthanized with isoflurane and the auditory cortex and surrounding temporal cortex (average weight of tissue ~20 mg) were dissected based on coordinates (Paxinos and Franklin 2004) and previous electrophysiological and dye-placement studies (Martin del Campo, Measor, & Razak, 2012). For an example of

auditory cortex dissection, please see Figure S2-1. The 1-hr time point was chosen based on the ~ 45 min half-life of SB-3CT (Gooyit et al., 2012). The AC was resuspended in lysis buffer (50mM Tris-HCL [pH = 7.4] buffer containing 150mM NaCl, 5mM EDTA, 0.05% Triton X-100, 1mM PMSF) containing protease inhibitor cocktail (Sigma-Aldrich, cat. #P8340) and phosphatase inhibitor cocktail (Sigma-Aldrich, cat. #P0044). Lysates were measured for total protein concentrations using the protocol for the BCA colorimetric protein assay (Pierce, cat. #23-235).

Lysates were diluted in reaction buffer and mixed with DQ-gelatin stock, a fluorescence-labeled gelatin substrate (Molecular Probes, E12055) as described previously (Lovelace et al., 2019). Lysates were coded and processed by experimenter blinded to codes. Fluorescence intensity was analyzed using 495 nm excitation wavelength and 515 nm emission wavelength in a fluorescence microplate reader equipped with standard fluorescein filters (SpectraMax M2, Molecular Devices). The signal from the samples was measured every 20 min during a 3-hr incubation period. For each time point, background fluorescence intensity was corrected by subtracting the values derived from the blank, which consisted of only reaction buffer and DQ gelatin. A standard curve to assess gelatinase activity was generated using recombinant mouse MMP-9 activity (rmMMP-9, specific activity approx. 1,500 pmol min⁻¹ μg⁻¹, R&D Systems, Cat. # 909-MM-010). A linear regression of rmMMP-9 activity (standard curve) and relative gelatinase activity based on the average fluorescence intensity of three replicates was used to assess gelatinase proteolytic activity in the lysates.

2.11 | Immunohistochemistry

For histology, mice were euthanized with isoflurane and perfused transcardially with ice-cold phosphate-buffered saline (0.1 M PBS, pH 7.4) and 4% paraformaldehyde (PFA). Brains were sectioned in the coronal plane on a Vibratome (Leica S1000) at 100 μm and sections were stored in PBS before staining. Prior to immunostaining, free-floating sections were post-fixed for an additional 2 hr in 4% PFA and then washed in 0.1M PBS. Sections were then quenched with 50mM ammonium chloride for 15 min, permeabilized with 0.1% Triton X-100 for 10 min, and blocked for 1 hr at 20–22°C in 5% donkey serum (DS; Sigma-Aldrich Cat# D9663, RRID:AB_2810235) and 1% bovine serum albumin (BSA; Fisher Scientific, Catalog #9048468) in 0.1 M PBS. Sections were incubated overnight in primary antibodies and a 1:500 dilution of fluorescein-tagged *Wisteria floribunda* Lectin (4 μg/ml WFA, Vector Laboratories Cat# FL-1351, RRID: AB_2336875) in a 1% DS, 0.5% BSA, and 0.1% Tween-20 solution. Primary antibodies included a 1:1,000 dilution of mouse anti-PV antibody (Sigma-Aldrich Cat#P3088, RRID:AB_477329) to label PV interneurons. Sections were incubated in a 1:500 dilution of donkey anti-mouse Alexa Fluor 594 for 1 hr. After immunostaining, sections were mounted on slides and cover slipped with Vectashield containing DAPI (Vector Laboratories Cat#H-1200, RRID:AB_2336790) and Cytoseal (ThermoScientific, Catalog #8310-16).

2.12 | Image quantification

Slices were imaged by confocal microscopy (model LSM 510, Carl Zeiss MicroImaging or Leica SP5) using a series of 10 high-resolution optical sections (1,024 × 1,024 pixel format) that were captured for each slice at 10 × magnification at 1 μm step intervals (z-stack). All images were acquired under identical conditions. Each z-stack was collapsed into a single image by projection, converted to a TIFF file, and encoded for blind analysis using ImageJ (NIH software, ImageJ, RRID:SCR_003070). The AC was identified using hippocampal landmarks (Figure S2-1). This method has been previously validated using tonotopic mapping and dye injection (Martin del Campo et al., 2012) and comparison with the Paxinos mouse atlas and other publications on the mouse AC (Anderson, Christianson, & Linden, 2009). Nevertheless, the precise boundary between primary AC (A1) and anterior auditory field (AAF) of the mouse AC cannot be clearly established. Both these fields are part of the lemniscal auditory system and comprise the core AC. Therefore, we use the AC to include both A1 and AAF. ImageJ was used to identify and count PNN-positive, PV-positive cells, and PV/PNN co-localization ($N = 6$ per group; vehicle-treated WT, $n = 18$; SB-3CT-treated WT, $n = 23$; vehicle-treated *Fmr1* KO, $n = 20$; SB-3CT-treated *Fmr1* KO, $n = 17$). Cortical layers were identified (Anderson et al., 2009) and used for layer-specific counts (Layers 1-5/6 of the AC). A selection tool was used to measure and specify layers of the AC and the point tool was used to label PNNs and PV cells and added to the ROI manager.

2.13 | Behavior

2.13.1 | Open-field test

Behavioral tests were performed as described previously (Lovelace et al., 2019; Sidhu et al., 2014). Briefly, anxiety-like behavior was tested in P27–28 mice ($N = 6–7$ per group) by quantifying their tendency to travel to the center of an open field and time spent in thigmotaxis (Yan, Asafo-Adjei, Arnold, Brown, & Bauchwitz, 2004; Yan, Rammal, Tranfaglia, & Bauchwitz, 2005). A 43 × 43 cm open-field arena with 43-cm-high walls was constructed from clear acrylic sheets. The open-field arena was placed in a brightly lit room, and one mouse at a time was placed in a corner of the open field and allowed to explore for 10 min while being recorded with digital video from above. The floor was cleaned with 3% acetic acid, 70% ethanol and water between tests to eliminate odor trails. The mice were tested between the hours of 8:00 a.m. and 1:00 p.m., and this test was always performed prior to the elevated plus maze by the same experimenter. The arena was subdivided into a 4 × 4 grid of squares with the middle of the grid defined as the center. A line 4 cm from each wall was added to measure thigmotaxis. Locomotor activity was scored by the analysis of total line crosses and speed as described previously with some modifications (Yan et al., 2005) using TopScan Lite Software (Clever Sys., Inc.). A tendency to travel to the center (total number of entries into large and small center squares) and the

time in thigmotaxis were used as an indicator of anxiety-like behaviors using TopScan Lite software (CleverSys Inc). The analysis was performed in 5-min intervals for the total 10-min exploration duration. Assessments of the digital recordings were performed blind to the condition. Statistical analysis was performed with unpaired *t* test using GraphPad Prism 6 software. Data represent mean \pm standard error of the mean (SEM).

2.13.2 | Elevated plus maze

The elevated plus maze consisted of four arms in a plus configuration. Two opposing arms had 15-cm tall walls (closed arms), and two arms were without walls (open arms). The entire maze sat on a stand 1 m above the floor. Each arm measured 30 cm long and 10 cm wide. Mice were allowed to explore the maze for 10 min while being recorded by digital video from above. The maze was wiped with 3% acetic acid, 70% ethanol and water between each test to eliminate odor trails. This test was always done following the open-field test. TopScan Lite software was used to measure the percent of time spent in open arms and speed. The time spent in open arm was used to evaluate anxiety-like behavior. The velocity and total arm entries were measured to evaluate overall locomotor activity. The analysis was performed in 5-min intervals for the total 10-min exploration duration. Assessments of the digital recordings were done blind to the condition using TopScan Lite software. Statistical analysis was performed with unpaired *t* test using GraphPad Prism 6 software. Data represent mean \pm standard error of the mean (SEM).

2.14 | Western blot analysis

Western blot analysis was performed as described previously (Lovelace et al., 2019). The AC was removed from each mouse ($N = 3-4$ mice per group), cooled in PBS, and homogenized in ice-cold lysis buffer (50 mM Tris-HCl, pH 7.4, 150 mM NaCl, 5 mM EDTA, 0.05% Triton X-100, and 1 mM PMSF) containing protease inhibitor cocktail (Sigma-Aldrich, cat. # P8340) and phosphatase inhibitor cocktail (Sigma-Aldrich, cat. #P0044). The samples were rotated at 4°C for at least 1 hr to allow for complete cell lysis and then cleared by centrifugation at 10,000 *g* for 15 min at 4°C. Supernatants were isolated and boiled in reducing sample buffer (Sigma-Aldrich, Laemmli 2 \times concentrate, S3401), and separated on 8%–16% Tris-Glycine SDS-PAGE precast gels (EC6045BOX, Life Technologies). Proteins were transferred onto Protran BA 85 Nitrocellulose membrane (GE Healthcare) and blocked for 1 hr at 20–22°C in 5% skim milk (catalog #170-6404, Bio-Rad). Primary antibody incubations were performed overnight at 4°C with antibodies diluted in TBS/0.1% Tween-20/5% BSA. The following primary antibodies were used: rabbit anti-Akt (Cell Signaling Technology Cat# 9272, RRID:AB_329827); rabbit anti-phospho-Akt (Ser473; Cell Signaling Technology Cat# 9271, RRID: AB_329825); mouse anti-PV (Millipore, Cat#MAB1572, RRID:AB_2174013), mouse anti-total TrkB (1:2000; BD Biosciences

Cat# 610101, RRID:AB_397507), rabbit anti-phospho-TrkB (Tyr515) (1:1,000, Bioworld, catalog #AP0236), and rabbit anti- β -actin at 1:2000 (Abcam Cat #ab8227, RRID:AB_2305186). All primary antibodies were from Cell Signaling Technology and used at a dilution of 1:1,000, unless stated otherwise.

Blots were washed 3 \times 10 min with TBS/0.1% Tween-20 and incubated with the appropriate HRP-conjugated secondary antibodies for 1 hr at 20–22°C in a TBS/0.1% Tween-20/5% BSA solution. The secondary antibodies used were HRP-conjugated donkey anti-mouse IgG (Jackson ImmunoResearch Labs Cat#715-035-150, RRID:AB_2340770) or HRP-conjugated goat anti-rabbit IgG (Jackson ImmunoResearch Labs Cat# 111-035-003, RRID:AB_2313567). After secondary antibody incubations, blots were washed 3 \times 10 min in TBS/0.1% Tween-20, incubated in ECL 2 Western Blotting Substrate (Thermo Scientific, catalog #80196) and a signal was collected with CL-XPosure film (Thermo Scientific, catalog #34090). For re-probing, membrane blots were washed in stripping buffer (2% SDS, 100 mM β -mercaptoethanol, 50mM Tris-HCl, pH 6.8) for 30 min at 55°C, then rinsed repeatedly with TBS/0.1% Tween-20, finally blocked with 5% skim milk, and then re-probed. Developed films were then scanned, and band density was analyzed by measuring band and background intensity using Adobe Photoshop CS5.1 software (Adobe Photoshop, RRID:SCR_014199). Four to five samples per group of vehicle versus. SB-3CT WT versus. *Fmr1* KO were run per blot. Statistical analysis was performed with unpaired *t* test using GraphPad Prism 6 software (GraphPad Prism, RRID:SCR_002798). Data represent mean \pm standard error of the mean (SEM).

2.15 | Statistical analysis

All statistical analyses for cell density quantification, Western blot, behavior, and DQ gelatin assay were done using Prism (GraphPad Software). For cell density quantification, theta/gamma ratio, and behavior, two-way ANOVA was used to compare Genotype (WT \times KO) versus. Treatment (SB-3CT \times vehicle) followed by *post hoc* pairwise comparisons with the Bonferroni's or Tukey's correction, unless otherwise specified. For Western blot and the DQ gelatin assay, the Student's *t* test was used to assess the effects of treatment in KO or WT mice. For all analyses, 'N' = number of animals and 'n' = number of coronal sections. No power analysis was performed to calculate sample size for each experiment. The number of animals for each study was determined using previously published studies using similar techniques [EEG (Lovelace et al., 2018; Wen, Lovelace, Ethell, Binder, & Razak, 2019), PV/PNN analysis (Lovelace et al., 2019; Wen et al., 2018), behavior, and DQ gelatin (Lovelace et al., 2019)].

3 | RESULTS

In the current study, we examined whether acute pharmacological inhibition of MMP-9 activity during a developmental critical period reduces auditory hypersensitivity in developing *Fmr1* KO mice. First,

we evaluated changes in spectral power and synchronization to auditory stimuli using EEG, as well as changes in PV/PNN density. Next, we assessed anxiety-like behaviors and hyperactivity along with changes in key molecular targets associated with FXS, including PV levels and phosphorylation of TrkB and Akt.

3.1 | Developing *Fmr1* KO mice exhibit increased resting state gamma EEG power and abnormal EEG power coupling

Previously, we have shown that adult *Fmr1* KO mice exhibit increased resting state gamma power (Lovelace et al., 2018), a phenotype that is similar to that observed in humans with FXS (Ethridge et al., 2017; Wang et al., 2017). Here, we assessed whether developing *Fmr1* KO mice on C57BL/6 background (for FVB background, see [Wen et al., 2019]) also exhibit increased resting state gamma power during the P21–28 period when maturation of various neuronal circuits occurs. To do this, mice were implanted with two-channel EEG electrodes placed in the auditory (AC) and frontal cortex (FC) at P18 (Figure 1a and b), allowed to recover for 4–5 days, and baseline EEG activity was recorded at P22 prior to treatment (PRE). Resting EEG data (in the absence of auditory stimulation) were collected for 5 min and were divided into 2-s segments for spectral analysis. Resting EEG raw power ($\mu\text{V}^2/\text{Hz}$) was calculated in the AC and FC of WT and *Fmr1* KO mice by analyzing all frequency bands during the entire 5-min resting period. Examples of one-second segments of EEG traces for individual WT and *Fmr1* KO mice are shown in Figure 1c and d, respectively (AC: top; FC: bottom). The group average power spectral densities for the AC and the FC are shown in histogram (Figure 1e) and bar graph format (Figure 1f), respectively. To normalize data for each region and to determine relative changes in power across frequency bands, power values were expressed as a ratio of *Fmr1* KO ($N = 20$) to WT ($N = 22$) means (for non-normalized data, see Figure S1–1). A value of 1 indicates no mean difference in power between WT and *Fmr1* KO, whereas values above 1 indicate *Fmr1* KO > WT, and below indicate *Fmr1* KO < WT mice.

Statistical analysis was performed using a one-way MANCOVA with the percentage of time spent moving as a covariate. We compared genotype mean differences on six bands per region: Delta (1–4 Hz), Theta (4–8 Hz), Alpha (8–13 Hz), Beta (13–30 Hz), Low Gamma (30–55 Hz), and High Gamma (65–100 Hz). Frequencies from 55 to 65 Hz were excluded in all analysis, as a 60 Hz notch filter was utilized to eliminate line noise. We confirmed assumptions of equality of covariance using Levene's test of equality of error variance and no differences between genotypes were observed in error variance (all $p > .05$). Since assumptions were not violated, we report an effect of genotype (AC: Pillai's Trace = 2.465, $p = .04$; FC: Pillai's Trace = 2.587, $p = .036$) across all six of the combined frequency variables. The low gamma band was the only frequency band significantly different between genotypes in the AC and FC (Figure 1f; AC: low gamma, $F(1,27) = 10$, $p = .003$, $\eta^2 = 0.204$, FC: low gamma, $F(1,27) = 9.012$, $p = .005$, $\eta^2 = 0.188$; WT $N = 22$, *Fmr1* KO $N = 20$;

for all frequency averages, see Table S1). These results indicate that *Fmr1* KO mice exhibit increased resting state low gamma power (30–55 Hz) early in development at P22–23.

Human EEG studies also report power abnormalities in delta, theta, alpha frequencies, and impaired coupling between low- and high-frequency oscillations in individuals with FXS and ASD (Sinclair et al., 2017; Wang et al., 2013). To determine whether there are abnormalities in power coupling in early development, a Pearson's correlation was done during the resting baseline period to assess the relationship between power across different frequencies and/or regions, using the same approach that was used in a study for human FXS (Wang et al., 2013). Results show a negative correlation in power coupling of the AC Theta/Low Gamma and AC Alpha/Low Gamma in WT mice (Figure 1g). These correlations were significantly reduced in *Fmr1* KO mice (T1G1: $p = .02$; A1G1: $p = .008$). Results also show a negative correlation in across region power coupling of the AC Theta/FC Low Gamma and AC Alpha/FC Low Gamma in WT mice (Figure 1i), and FC Theta/AC Low Gamma and FC Alpha/AC Low Gamma (Figure 1j). These correlations were also significantly reduced in *Fmr1* KO mice (T1G2: $p = .03$; A1G2: $p = .04$; T2G1: $p = .04$; A2G1: $p = .03$).

Overall, these findings indicate that abnormalities in resting gamma power and EEG power coupling, in particular changes in theta/low gamma and alpha/low gamma power coupling in the AC and cross regional impairments, are present in developing *Fmr1* KO mice as early as P22–23.

3.2 | *Fmr1* KO mice treated with MMP-9 inhibitor show no effect on resting state EEG gamma power and EEG power coupling

Next, both *Fmr1* KO and WT mice received a single i.p. injection of the MMP-2/9 inhibitor, SB-3CT (25 mg/kg), or vehicle immediately following EEG recording to assess the efficacy of acute MMP-9 inhibition to normalize resting EEG oscillation pattern (Figure 1a). One day after treatment, resting EEG baseline data were again collected for 5 min and was divided into 2-s segments for spectral analysis. The percentage of time that the mice spent moving during the recording period was not different between genotypes (Figure S1–2) or treatment groups (Figure S2–7). Figure 2 shows the average spectral power as a ratio of the corresponding control group in histogram (Figure 2a–c) and bar graph format (Figure 2d–f) for each group (AC: top; FC: bottom; for non-normalized data see Figure S2–2). To determine resting EEG in vehicle groups, vehicle-treated *Fmr1* KO mice were compared to vehicle-treated WT mice. Although resting state low (LG) and high gamma (HG) power was trending higher in the AC of vehicle-treated *Fmr1* KO ($N = 12$) compared to vehicle-treated WT ($N = 16$) mice, this was not statistically significant possibly due to large variability in vehicle-injected *Fmr1* KO mice (Figure 2d; also see Figure S2–4). Although SB-3CT-treated *Fmr1* KO ($N = 12$) mice exhibited normal low and high gamma in the AC and FC that was comparable to SB-3CT-treated WT ($N = 15$) mice (Figure 2e), comparison of SB-3CT-treated *Fmr1* KO ($N = 12$) mice to vehicle-treated *Fmr1* KO ($N = 12$) mice showed

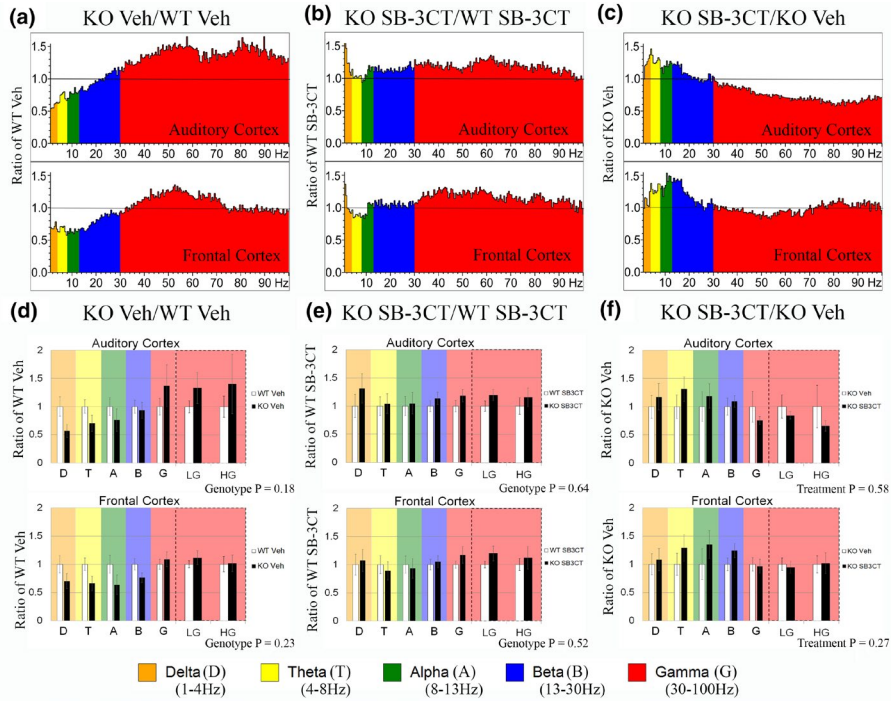


FIGURE 2 Effects of acute inhibition of MMP-9 activity on resting EEG power in *Fmr1* KO mice. Five minutes of resting EEG activity was recorded from WT and *Fmr1* KO mice post-treatment at P23-24 (from treatment groups, $N = 2$ from vehicle-treated WT and *Fmr1* KO groups, respectively, and $N = 1$ from the SB-3CT-treated *Fmr1* KO group was excluded from resting baseline EEG analysis). FFT calculated spectral power ($\mu V^2/Hz$) for each group is shown as a ratio of a corresponding control group. (a and d) Average power in the AC (top) and FC (bottom) of vehicle-treated *Fmr1* KO ($N = 14$, excluded $N = 2$) compared to vehicle-treated WT ($N = 18$, excluded $N = 2$). (b and e) Average power in the AC and FC of SB-3CT-treated *Fmr1* KO ($N = 13$, excluded $N = 1$) compared to SB-3CT-treated WT ($N = 15$, no excluded animals). (c and f) Average power of SB-3CT-treated *Fmr1* KO compared to vehicle-treated *Fmr1* KO. All graphs represent average values and the error bars indicate SEM. Delta (D), Theta (T), Alpha (A), Beta (B), Low Gamma (LG), and High Gamma (HG)

a trending reduction in low and high gamma power, but this was not statistically significant (Figure 2f; for summary of all frequency averages, see Table S2). Vehicle-treated WT mice ($N = 16$) and SB-3CT-treated WT mice ($N = 15$; for non-normalized data, see Figure S2-3) did not show any significant changes in spectral frequencies compared to WT mice before treatment (PRE) in AC or FC (Figure S2-5a and 2-5d [Vehicle-WT] and Figure S2-5b and 2-5e [SB-3CT-WT]).

To determine whether EEG power coupling abnormalities were ameliorated following treatment with SB-3CT, a Pearson's correlation was done during the resting baseline period to assess the relationship between power across different frequencies and/or regions. Results show that treatment with SB-3CT did not alter the EEG power coupling profiles in WT or *Fmr1* KO mice (Figure S2-6).

Together, these results indicate no significant effects of treatment in *Fmr1* KO mice when resting EEG power or EEG power coupling was analyzed for individual frequencies between vehicle- and SB3CT-treated groups.

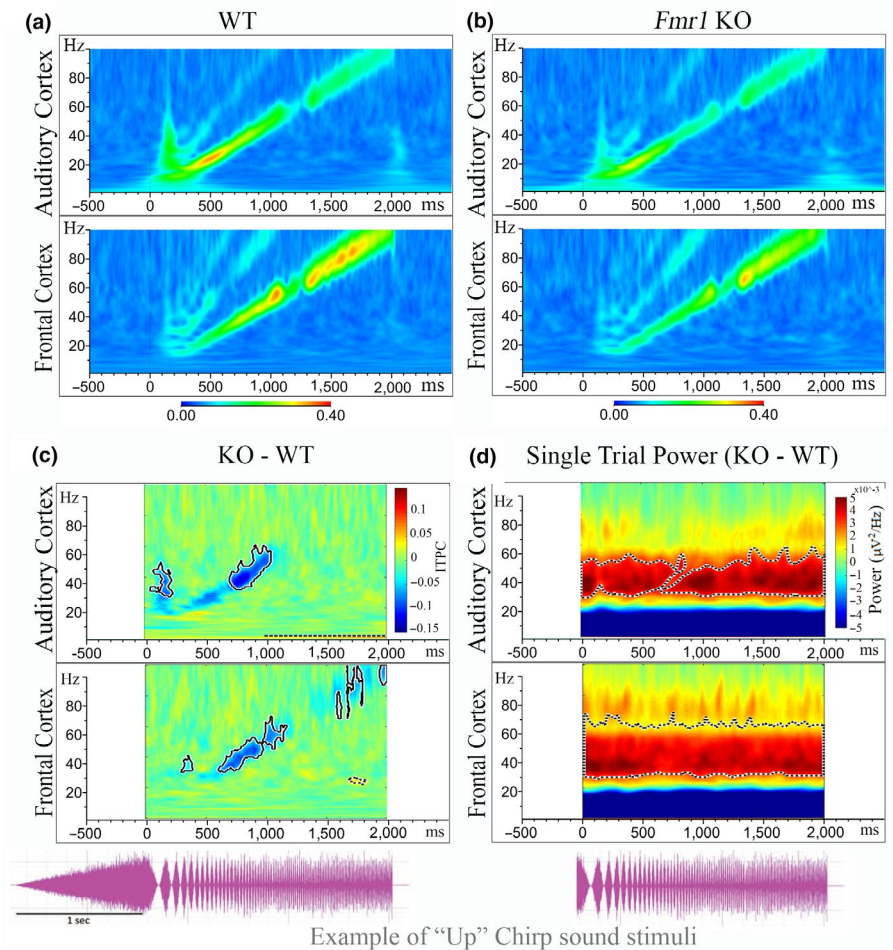
3.3 | Phase locking to auditory 'up chirp' stimuli is impaired in developing *Fmr1* KO mice

To assess whether P22-23 *Fmr1* KO mice also exhibit deficits in the consistency of phase locking to time-varying stimuli as seen in adult

Fmr1 KO mice (Lovelace et al., 2018), and humans with FXS (Ethridge et al., 2017), we recorded responses to chirp stimuli. We tested both Up- and Down-chirpstimuli to ensure that the differences are specific to modulation frequencies and are not affected by the direction of frequency change in the sound (Lovelace et al., 2019). Following EEG resting state baseline recording, repeated chirp stimuli (300 trials for up, 300 trials for down) was delivered and electrocortical activity was recorded. Inter-trial phase coherence (ITPC) was calculated across trials in the time \times frequency domain using Morlet Wavelet analysis (Lovelace et al., 2018). After grand average ITPC was calculated for each group, we found EEG oscillations that matched the frequency of the chirp and were seen as increased ITPC along a diagonal, from 0 to 2 s and 1-100 Hz. The means for WT PRE (Figure 3a; only 'up chirp' data are shown) were subtracted from *Fmr1* KO PRE mice (Figure 3b) to show the difference between *Fmr1* KO and WT (Figure 3c) in the AC (top) and FC (bottom). For statistical analysis, clusters of p values were calculated, and significant differences ($p < .025$) were overlaid on the chirp response to demonstrate quantitative differences between each genotype after correction for multiple comparisons (Lovelace et al., 2019). We observed a statistical difference between genotypes in one main cluster, which spans the low gamma band ITPC in both the AC (35-55 Hz) and FC (35-65 Hz); significant clusters are highlighted by bold-lined contours in Figure 3c. In the FC, there was also a statistical difference between genotypes in the high gamma band in the FC



FIGURE 3 *Fmr1* KO mice are deficient in phase locking to auditory ‘UpChirp’ stimuli. (a and b) Inter-Trial Phase Coherence (ITPC: ability to synchronize oscillations to stimulus frequencies) grand average for WT ($N = 23$) and *Fmr1* KO ($N = 19$) mice in the AC (top) and FC (bottom). EEG oscillations matched the frequency of the chirp and were seen as increased ITPC along a diagonal, from 0 to 2 s and 1–100 Hz. (c) ITPC means for WT PRE were subtracted from *Fmr1* KO PRE mice to show the difference between genotypes. Blue areas indicating $KO < WT$, green areas no difference, and yellow/red $KO > WT$. Significant clusters ($p < .025$) are highlighted by bold-lined contours. (d) Graph shows difference in grand average single trial power (STP) or ongoing ‘background’ power during auditory stimulation between WT PRE and *Fmr1* KO mice in AC (top) and FC (bottom)



(80–100 Hz). Similar patterns of statistics of ITPC were observed for both up and down chirps (down chirp data not shown).

To examine whether P22–23 *Fmr1* KO mice also exhibit an increase in background gamma power in both the AC and FC during the chirp presentation, similar to adult *Fmr1* KO mice (Lovelace et al., 2018), we assessed non-phase locked single trial power (STP) during chirp stimulation in *Fmr1* KO mice compared to WT control mice. Using the same statistical cluster analysis as for the chirp ITPC, results indicate that P22–23 *Fmr1* KO mice exhibit a significant increase in background gamma power in the AC (~30–55 Hz) and FC (~30–70 Hz) compared to WT control mice (Figure 3d).

Together, these data show that developing *Fmr1* KO mice exhibit low and high gamma synchronization deficits and increased background gamma power in both the AC and FC in a manner similar to adult *Fmr1* KO mice and humans with FXS.

3.4 | Acute MMP-9 inhibition improves phase-locking to time-varying auditory stimuli in *Fmr1* KO mice

To test whether acute treatment of SB-3CT would ameliorate the ITPC deficit to the auditory chirp stimuli, both up and down chirps were presented during EEG recording 1 day after treatment. Figure 4a and b shows the grand average ITPC values for

vehicle-treated and SB-3CT-treated *Fmr1* KO, respectively. The mean for vehicle-treated *Fmr1* KO mice was subtracted from vehicle-treated WT mice (Figure 4c) to show the difference between ITPC values in *Fmr1* KO and WT mice in both the AC and FC. Similarly, the mean for SB-3CT-treated *Fmr1* KO mice was subtracted from the mean of vehicle-treated *Fmr1* KO mice (Figure 4d). For statistical analysis, clusters of p values were calculated, and these differences were overlaid on the chirp response to demonstrate quantitative differences between each genotype after correction for multiple comparisons. Monte Carlo statistical method on cluster analysis revealed a significant reduction in average ITPC values between vehicle-treated *Fmr1* KO ($N = 12$) mice and vehicle-treated WT ($N = 17$) mice in low gamma band range (~40–50 Hz) in the AC (Figure 4c: top), consistent with the reduction observed in un-treated mice (Figure 3d). Statistical analysis of average ITPC values shows a significant enhancement in the same low gamma band range (~40–50 Hz) ITPC in the AC of SB-3CT-treated *Fmr1* KO mice ($N = 12$) to vehicle-treated *Fmr1* KO ($N = 12$) mice (Figure 4d: top). However, a significant decrease in ~30–40 Hz gamma band range ITPC band in both AC and FC was observed (time \times frequency bands that are significantly different between groups are highlighted in bolded black lines). Grand average ITPC values were also calculated for vehicle-treated ($N = 17$) and SB-3CT-treated WT ($N = 14$) mice (Figure S4-1a and S4-1b,

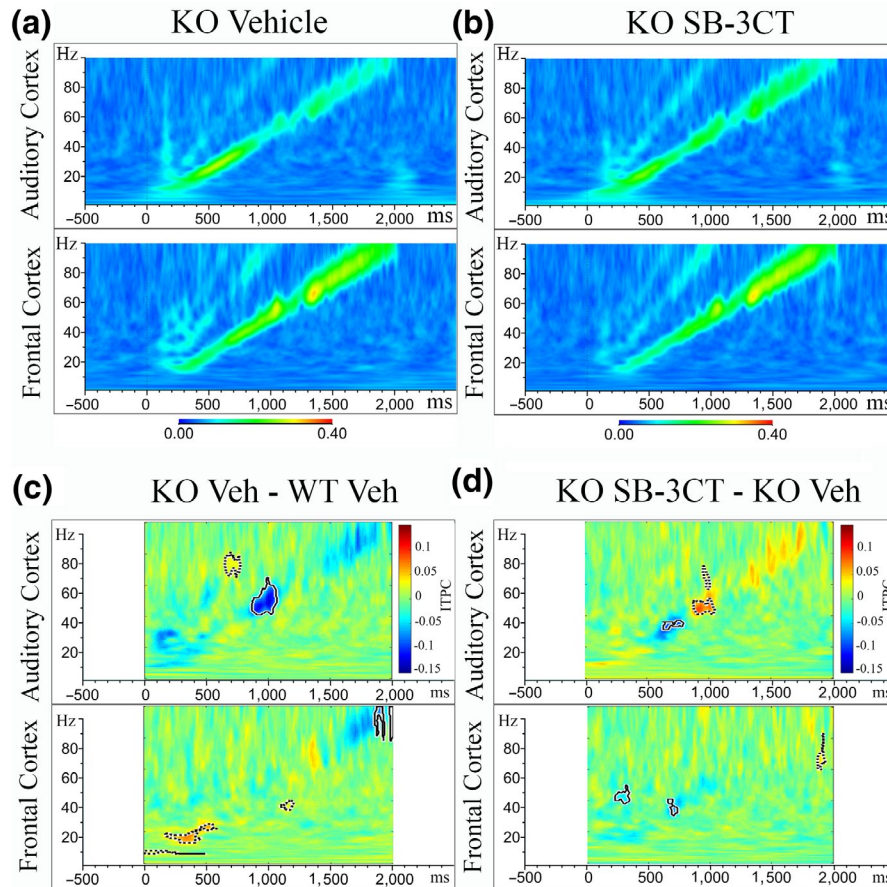


FIGURE 4 Acute SB-3CT treatment improves Inter-Trial Phase Coherence (ITPC) to auditory ‘Up Chirp’ stimuli in *Fmr1* KO mice. (a and b) Grand average ITPC in AC and FC of vehicle-treated *Fmr1* KO (a, $N = 12$) and SB-3CT-treated *Fmr1* KO (b, $N = 12$). Warmer colors, yellow/red, represent high ITPC values, while cooler colors, blue/green, represent low ITPC values. Significant clusters ($p < .025$) are highlighted by bold-lined contours. (c) Graph shows the difference in ITPC values between vehicle-treated *Fmr1* KO ($N = 12$) and vehicle-treated WT ($N = 17$). (d) Graph shows the difference in ITPC values between SB-3CT-treated *Fmr1* KO ($N = 12$) and vehicle-treated *Fmr1* KO ($N = 12$)

respectively). No significant differences were detected in AC or FC for average ITPC values between vehicle-treated WT ($N = 17$) mice and WT PRE ($N = 23$) mice in the low and high gamma ITPC band except for a small decrease in the FC at ~ 25 – 35 Hz (Figure S4-1c), suggesting the effects of injection on the ~ 25 – 35 Hz gamma band range. SB-3CT-treated WT ($N = 14$) mice exhibited a significant increase in high gamma band ITPC in the AC, but not FC, specifically in 70–85 Hz ITPC band compared to WT PRE (Figure S4-1d). Similar patterns and statistics of ITPC were observed for both up and down chirps. These results indicate that an acute treatment of the MMP-9 inhibitor, SB-3CT, improves fidelity of temporal responses to auditory stimuli by specifically increasing low gamma band (40–50 Hz) ITPC in developing *Fmr1* KO mouse cortex.

3.5 | Acute inhibition of MMP-9 enhances PNN formation in the developing auditory cortex of *Fmr1* KO mice

Previously, we showed evidence for delayed development of PV interneurons and PNN formation around PV interneurons in layers

2–4 of the developing AC of *Fmr1* KO mice (Wen et al., 2018). Here, we examined whether acute pharmacological inhibition of MMP-9 would ameliorate the PV/PNN deficits in P22–23 *Fmr1* KO mice. To test this, immediately after EEG recordings (1 day after treatment), mice were sacrificed, and brains were collected for PV immunostaining and PNN labeling using *Wisteria floribunda* Agglutinin (WFA; Figure 1a, PV/PNN analysis). We analyzed the density of PV-positive (Figure 5a, e, i, m), PNN-positive (Figure 5b, f, j, 5n), and PV/PNN co-labeled neurons (Figure 5c, g, k, o) in layer 4 of the AC contralateral to the EEG electrode (for layers 1, 2/3, and 5/6, see Figure S5-1). We observed a significant increase in PNN density in SB-3CT-treated *Fmr1* KO mice compared to vehicle-treated *Fmr1* KO mice (Figure 5r, $p = .02$). There was also a significant increase of PNN density in SB-3CT-treated WT mice compared to vehicle-treated WT mice (Figure 5r, $p = .009$). Statistical analysis of PV/PNN co-localization revealed a significant increase in PV/PNN co-localization in SB-3CT-treated *Fmr1* KO mice compared to vehicle-treated *Fmr1* KO mice (Figure 5s, $p = .008$). There was also a significant increase in PV/PNN co-localization in SB-3CT-treated WT mice compared to vehicle-treated WT mice (Figure 5s, $p = .04$; for all average values and statistics, see Tables S3 and S4).

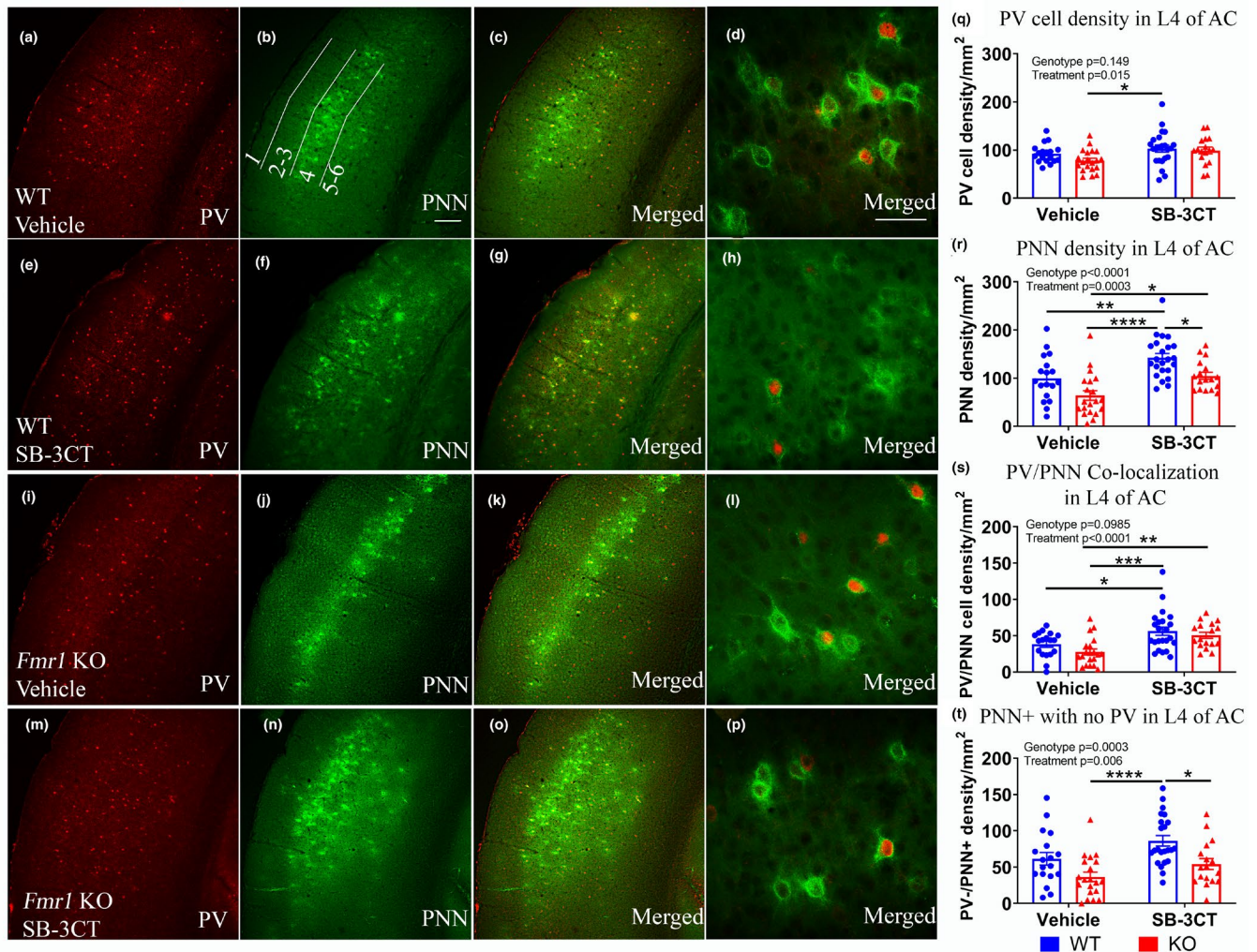


FIGURE 5 Acute SB-3CT treatment enhances PNN formation around PV cells in layer 4 auditory cortex of *Fmr1* KO mice. Confocal images of PV immunoreactivity (red; a, e, i, m), PNN labeling with WFA (green; b, f, j, n) and PV/PNN double labeling (c, g, k, o) in vehicle-treated WT (a–d), SB-3CT-treated WT (e–h), vehicle-treated *Fmr1* KO (i–l), and SB-3CT-treated *Fmr1* KO (m–p). Scale bar, 150 μ m (b). High-magnification images of PV/PNN in vehicle-treated WT (d), SB-3CT-treated WT (h), vehicle-treated *Fmr1* KO (l), and SB-3CT-treated *Fmr1* KO (p). Scale bar, 50 μ m. (q–t) Graphs show density of PV cells (q), PNN-positive cells (r), PV/PNN co-localization (s) and PV-negative cells with PNN (t). All graphs represent average values and the error bars indicate SEM ($n = 17$ –23 per group, $N = 6$ per group; * $p < .05$; ** $p < .01$; *** $p < .001$; **** $p < .0001$)

Taken together, these data suggest that acute pharmacological inhibition of MMP-9 normalizes PNN development and co-localization of PNN predominantly around PV interneurons in layer 4 of the developing AC of *Fmr1* KO mice, consistent with improved phase locking at low gamma band frequencies.

3.6 | Acute inhibition of MMP-9 ameliorates anxiety and hyperactivity in *Fmr1* KO mice

Next, we assessed whether SB-3CT treatment reduces anxiety-like behaviors and hyperactivity in *Fmr1* KO mice that received an i.p. injections of SB-3CT (25 mg/kg) at P27–28 (for timeline, see Figure 6a). Anxiety-like behaviors were assessed on P28–29 mice (1 day after treatment) using the elevated plus maze (EPM)

and open field (OF). In the EPM, mice were allowed to explore the cross-shaped field for 10 min. TopScan Live software was used to evaluate anxiety-like behaviors by determining the percent of time spent in the open arms (Figure 6b). To evaluate locomotor activity and hyperactivity, the number of total entries into open and closed arms (Figure 6c), and the average speed (Figure 6d) were quantified. Results showed that vehicle-treated *Fmr1* KO mice spent less time in the open arms compared to vehicle-treated WT controls (Figure 6b). Statistical analysis using two-way ANOVA revealed significant effect of treatment, genotype, and significant interaction (for statistical comparisons, refer to Table S5). Post hoc comparisons showed that SB-3CT-treated *Fmr1* KO mice spent more time in open arms than vehicle-treated *Fmr1* KO mice (Figure 6b, $p < .0001$). Treatment with SB-3CT did not alter behavior of WT mice, suggesting specificity of the drug to the *Fmr1* KO group.

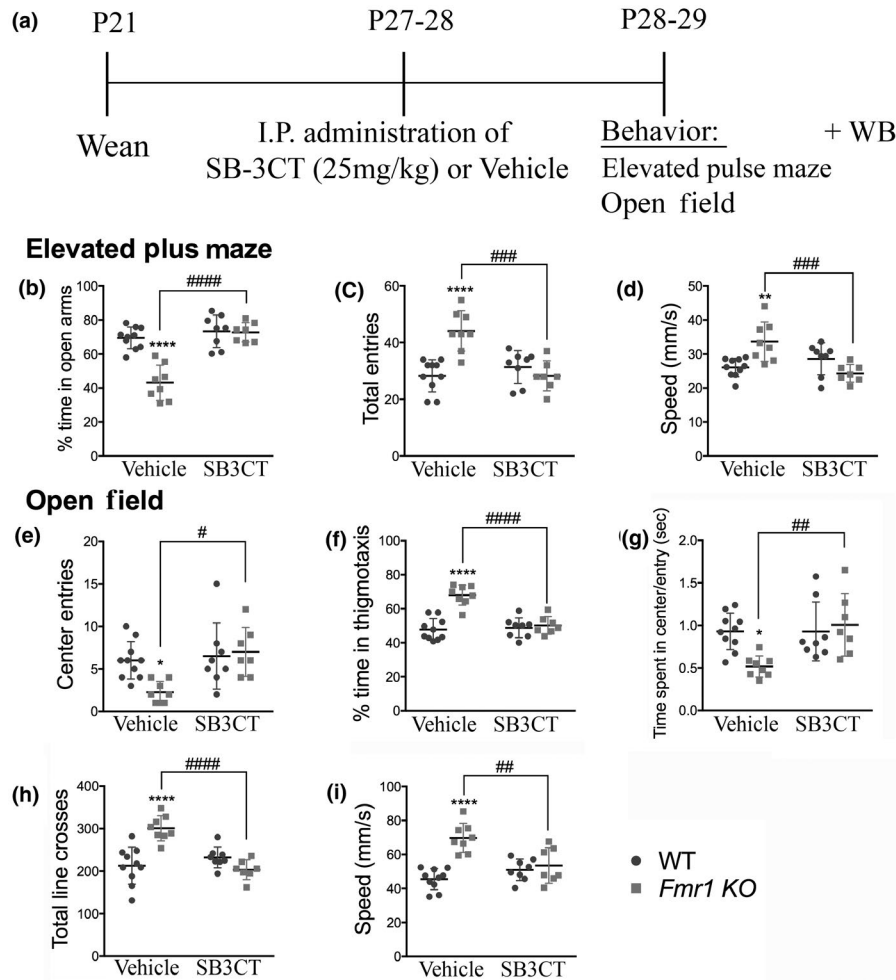


FIGURE 6 Acute SB-3CT-treatment normalizes anxiety/hyperactivity phenotype associated with *Fmr1* KO mice. (a) Experimental timeline for behavior and Western blot analysis. For this, mice were given either an intraperitoneal injection of SB-3CT (25 mg/kg) or vehicle at P27–28 and were tested for anxiety, locomotor, and hyperactivity using the open field and elevated plus maze test 1-day post-treatment. Brain samples were collected for Western blot analysis immediately after behavior. (b–d) Graphs show the percent time spent in the open arms (b), total entries into open and closed arms (c), and the average speed (d) in the elevated plus maze. (e–i) Graphs show the total number of center entries (e), the percent time spent in thigmotaxis (f), the time spent in the center per entry (g), the total number of line crosses (h), and the average speed (i) in the open-field test. All graphs represent average values and the error bars indicate SEM (WT vs. *Fmr1* KO: * $p < .05$, ** $p < .01$, **** $p < .0001$; vehicle-treated versus SB-3CT-treated *Fmr1* KO: # $p < .05$, ## $p < .01$, ### $p < .001$, #### $p < .0001$, ##### $p < .00001$, vehicle-treated WT, $N = 10$; SB-3CT-treated WT, $N = 8$; vehicle-treated *Fmr1* KO, $N = 10$; SB-3CT-treated *Fmr1* KO, $N = 9$)

Vehicle-treated *Fmr1* KO mice also showed an increase in the number of total entries (Figure 6c, $p = .0001$) and speed (Figure 6d, $p = .0030$) compared to vehicle-treated WT controls. Treatment of *Fmr1* KO mice with SB-3CT reduced the number of total entries (Figure 6c, $p = .0001$) and speed (Figure 6d, $p = .0008$), yet it did not significantly alter the number of total entries or speed in WT controls (Figure 6c and d).

In the OF task, animals were allowed to explore an open field for 10 min. Anxiety-like behaviors were evaluated by measuring the total number of center entries (Figure 6e), the percent of time spent in thigmotaxis (Figure 6f), and the time spent in the center per entry (Figure 6g). Locomotor activity was assessed by determining the number of total line crosses (Figure 6h) and average speed (Figure 6i). All behaviors were quantified using TopScan Live software. Statistical analysis using two-way ANOVA revealed significant

main effects of treatment and interaction (for statistical comparisons, refer to Tables S5 and S6). Post hoc comparisons showed that vehicle-treated *Fmr1* KO mice made fewer center entries (Figure 6e, $p = .0316$), spent more time in thigmotaxis (Figure 6f, $p < .0001$) and spent less time in the center per entry (Figure 6g, $p = .0173$) compared to vehicle-treated WT controls. However, SB-3CT-treated *Fmr1* KO mice made more center entries (Figure 6e, $p = .0101$), spent less time in thigmotaxis (Figure 6f, $p < .0001$) and more time in the center per entry (Figure 6g, $p = .0086$) compared to vehicle-treated *Fmr1* KO mice. Statistical analysis using two-way ANOVA also revealed a significant increase in the total line crosses (Figure 6h, $p < .0001$) and average speed (Figure 6i, $p < .0001$) in vehicle-treated *Fmr1* KO mice compared to vehicle-treated WT mice. SB-3CT treatment significantly decreased the total line crosses (Figure 6h, $p < .0001$) and average speed (Figure 6i, $p = .0021$; for all average

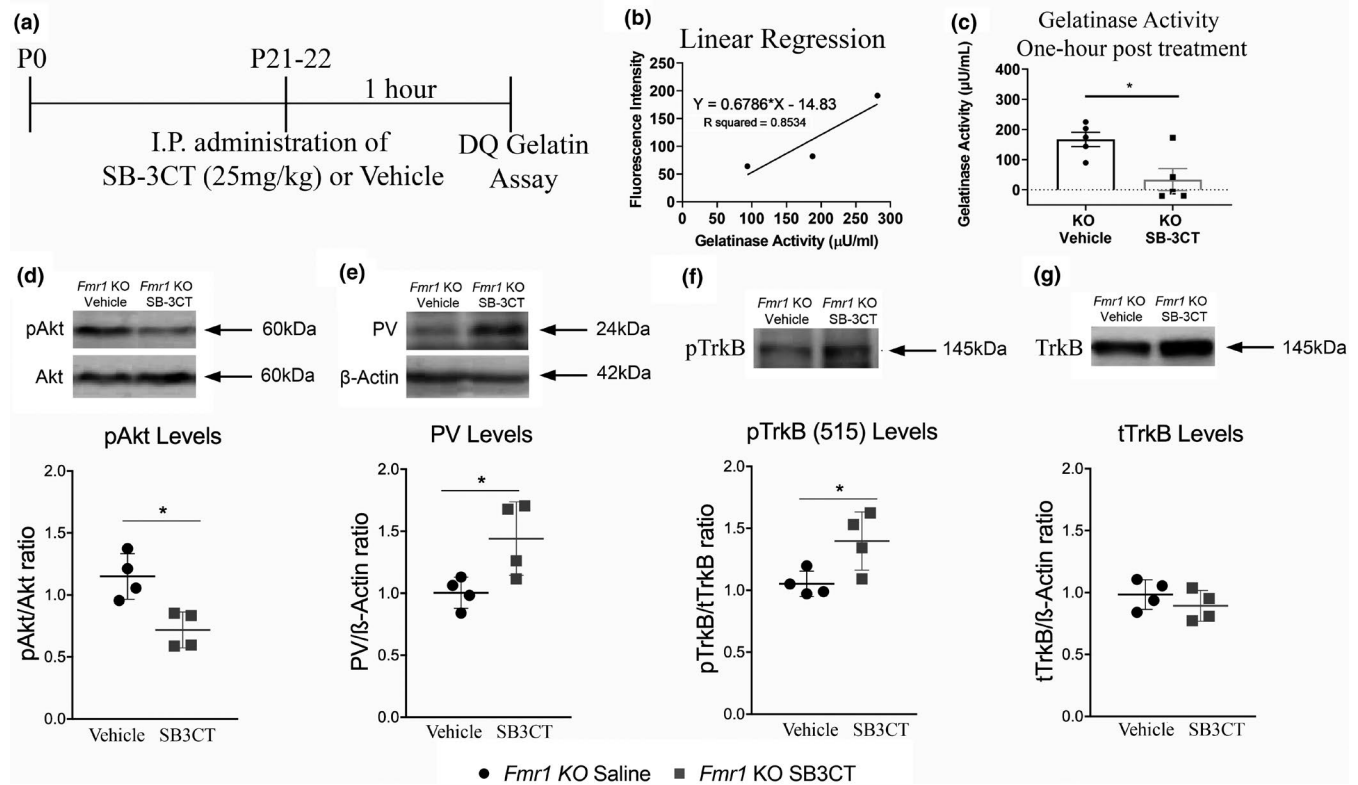


FIGURE 7 Acute MMP-9 inhibition reduces gelatinase activity and phosphorylation of Akt while increasing PV levels and phosphorylation of TrkB in the AC of *Fmr1* KO mice. To confirm that the MMP-2/9 inhibitor, SB-3CT, reduced MMP-2/9 activity following treatment, gelatinase activity was measured using a Dye-Quenched (DQ) gelatin assay. (a) Experimental timeline for DQ gelatin assay. Mice (no EEG) were given either an intraperitoneal injection of SB-3CT (25 mg/kg) or vehicle at P21–22 and brains were collected for the DQ Gelatin assay 1-hr post-injection. (b) Graph shows standard curve. (c) *Fmr1* KO mice injected with SB-3CT (25 mg/kg) show reduced gelatinase activity compared to vehicle-treated mice 1-hr post-injection ($N = 5$ per group, t test, $p = .02$). (d–g) Western blots show levels of pAkt and Akt (d), PV and actin (e), pTrkB515 (f), and TrkB (d). Graphs show pAkt/Akt (d), PV/actin (e), pTrkB515/TrkB (f), and TrkB/actin (g) ratios in the AC of vehicle-treated and SB-3CT-treated *Fmr1* KO mice ($N = 4$ per group) 24-hr post-injection. All graphs represent average values and error bars indicate SEM ($*p < .05$)

values and statistics, see Tables S5 and 6) of *Fmr1* KO mice. SB-3CT treatment did not change the behavior of WT mice in the open field.

These results suggest that acute inhibition of MMP-9 using SB-3CT alleviates anxiety/hyperactivity observed in *Fmr1* KO mice, without altering these behaviors in WT mice.

3.7 | Acute inhibition of MMP-9 with SB-3CT reduces gelatinase activity and phosphorylation of AKT while increasing PV levels and phosphorylation of TRKB

To confirm that the MMP-2/9 inhibitor, SB-3CT, reduced MMP-2/9 activity following treatment, gelatinase activity was measured using a Dye-Quenched (DQ) gelatin assay. *Fmr1* KO mice were injected with SB-3CT (25 mg/kg) or vehicle, the auditory and surrounding temporal cortex (Figure S2–1) was collected and homogenized for the DQ gelatin assay 1-hr post-injection (for timeline, see Figure 7a). A mouse recombinant MMP-9 ($\sim 1,500 \text{ pmol min}^{-1} \mu\text{g}^{-1}$) was used as a standard to calculate the approximate MMP-9 activity in the sample using a linear regression curve (Figure 7b). Results reveal that SB-3CT-treated *Fmr1* KO mice exhibit significantly decreased levels of

gelatinase activity 1-hr post-injection compared to vehicle-treated *Fmr1* KO mice (Figure 7c, t test, $N = 5$ per group, $p = .02$, Table S7). SB-3CT-treated WT mice also show significantly reduced gelatinase activity compared to vehicle-treated WT mice (Figure S7–1).

Previous studies have shown over-activation and enhanced phosphorylation of Akt/mTOR in the cortex of *Fmr1* KO mice (Lovelace et al., 2019) may underlie abnormalities in synaptic functions and hyperexcitability (Klann & Dever, 2004; Sharma et al., 2010). In addition, genetic deletion of MMP-9 restored Akt/mTOR phosphorylation to the normal levels in the hippocampus of *Fmr1* KO mice, while treatment of WT neurons with active MMP-9 enhanced Akt/mTOR phosphorylation (Sidhu et al., 2014). Therefore, to determine whether acute pharmacological MMP-9 inhibition influenced Akt/mTOR-related signaling, we analyzed Akt phosphorylation in the AC of SB-3CT and vehicle-treated *Fmr1* KO mice. *Fmr1* KO mouse brains were collected for Western blot analysis at P27–28 immediately after behavior, 1 day following treatment (for timeline see Figure 6a). Results show reduced levels of Akt phosphorylation in SB-3CT-treated *Fmr1* KO mice compared to vehicle-treated *Fmr1* KO mice (Figure 7d; $N = 4$, $t(6) = 4.274$, $p = .0235$, t test). There were no significant changes in Akt phosphorylation in SB-3CT-treated compared to vehicle-treated WT mice (Figure S7–2a).



As TrkB signaling is implicated in PV cell development and survival (Nomura et al., 2017; Xenos et al., 2018), we examined the effects of acute MMP-9 inhibition on PV levels and phosphorylation of TrkB using Western blot. Results show that following SB-3CT treatment *Fmr1* KO mice exhibit increased PV levels (Figure 7e; $N = 4$, $t(6) = 2.607$, $p = .0479$, t test). We also observed an increase in TrkB phosphorylation on Tyrosine (Y) 515 in SB-3CT-treated *Fmr1* KO mice compared to vehicle-treated *Fmr1* KO mice (Figure 7f; $N = 4$, $t(6) = 2.805$, $p = .0378$, t test), while there was no significant change in total TrkB levels (Figure 7g; for average values, see Table S8). Comparison of SB-3CT-treated WT versus vehicle-treated WT mice did not reveal any significant changes in PV (Figure S7-2b), pTrkB_{Y515} (Figure S7-2c), or total TrkB (Figure S7-2d).

4 | DISCUSSION

In this study, we show that P22–23 *Fmr1* KO mice exhibit abnormal neural oscillation patterns that parallel adult *Fmr1* KO mice and humans with FXS including increased resting state gamma power and deficits in gamma synchronization to auditory stimuli. Treatment with the MMP-9 inhibitor, SB-3CT, had no significant effect on resting EEG power or EEG power coupling in *Fmr1* KO mice. However, acute inhibition of MMP-9 activity improved fidelity of gamma frequency (~40 Hz) phase locking to time-varying auditory stimuli in SB-3CT *Fmr1* KO mice compared to vehicle-treated *Fmr1* KO mice. At the molecular level, SB-3CT treatment enhanced PNN formation predominantly around PV interneurons in the developing AC of both *Fmr1* KO mice and WT mice. Assessment of anxiety/hyperactivity with EPM and OF tests demonstrated that acute inhibition of MMP-9 activity ameliorated anxiety-like behaviors and hyperactivity in *Fmr1* KO mice. Lastly, acute inhibition of MMP-9 activity reduced Akt phosphorylation while increasing PV levels and TrkB phosphorylation. Our data are consistent with previously reported benefits of minocycline treatment in humans with FXS (Schneider et al., 2013), *Fmr1* KO mice (Bilousova et al., 2009; Dansie et al., 2013; Toledo, Wen, Binder, Ethell, & Razak, 2019), and the *Drosophila* FXS model (Siller & Broadie, 2011), and further suggest that minocycline may alleviate FXS symptoms by suppressing MMP-9. These data support the notion that cellular and electrophysiological abnormalities of sensory processing are present early in development. In addition, treatment during early postnatal developmental period may be beneficial in ameliorating deficits due to higher cortical plasticity. Furthermore, reduction of MMP-9 activity may provide a suitable target to reduce auditory hypersensitivity in FXS and potentially other ASDs.

4.1 | Developing and adult *Fmr1* KO mice exhibit comparable EEG phenotypes

In this study, we show that developing *Fmr1* KO mice (P22–23) exhibit increased resting state low gamma power in both the

AC and FC (Figure 1) similar to adult *Fmr1* KO mice. Unlike adult *Fmr1* KO mice, though, developing *Fmr1* KO mice do not exhibit increased resting state delta or high gamma power (Lovelace et al., 2018). These results are consistent with data from the FVB strain of mice (Wen et al., 2019), suggesting that abnormal electrophysiological phenotypes are observed as early as P22 in developing *Fmr1* KO mice. The consistency of EEG phenotypes across age and genetic backgrounds of mice, and between humans and mice, indicates that these measures can be utilized as objective physiological biomarkers to test the effectiveness of potential drugs. Furthermore, accumulating evidence indicates that increased resting state gamma power is associated with sensory processing and communication deficits in FXS and ASD (Ethrige et al., 2017, 2019; Lovelace et al., 2018, 2019; Sinclair et al., 2017; Wang et al., 2017). Additional studies also point to abnormalities in theta and alpha power as contributing mechanisms underlying hyperexcitability (Van der Molen & Van der Molen, 2013). Theta power is linked to cortical arousal level (Barry, Clarke, Johnstone, McCarthy, & Selikowitz, 2009). Alpha power has been interpreted to reflect a neural inhibitory mechanism that regulates the processing of external, sensory information (Klimesch, 1999; Mathewson et al., 2011). In particular, GABAergic inhibitory activity is thought to contribute to this neural inhibition mediated by alpha oscillations (Jensen & Mazaheri, 2010). Together, alpha/theta synchronization has been linked to cognitive function (Klimesch, 1999) and ability to inhibit irrelevant sensory information (Van der Molen & Van der Molen, 2013). Human EEG studies report an inverted U-shaped pattern of power abnormalities showing reduced alpha frequencies, but increased delta, theta frequencies and high-frequency bands (beta, gamma) in children with ASD (Sinclair et al., 2017; Wang et al., 2013). Elevated theta and delta power and reduced alpha power is also observed in individuals with ADHD (Barry, Johnstone, & Clarke, 2003; Born et al., 2017). Our study shows a reduced EEG power correlations between Theta and Low Gamma, Alpha and Low Gamma bands within the AC as well as across regions (AC to FC and FC to AC) in *Fmr1* KO mice compared to WT mice. Overall, our findings indicate that abnormalities in EEG oscillation pattern, which are associated with hyperexcitability, cognitive performance, and ability to process sensory information, are present in developing *Fmr1* KO mice as early as P22–23.

In this study, we show that developing *Fmr1* KO mice exhibit decreased ability to produce synchronous stimulus-induced oscillations, similar to adult *Fmr1* KO mice (Lovelace et al., 2018), but the impairment is localized specifically to the low gamma frequencies (~30–55 Hz) in the AC and both low and high gamma (~65–100 Hz) frequencies in the FC. Treatment of *Fmr1* KO mice with SB-3CT leads to an improvement in phase locking to auditory chirp stimuli, in the same frequency range (~40–50 Hz) where the deficit was observed in vehicle-treated *Fmr1* KO AC (Figure 4). This result indicates that SB-3CT may be targeting specific cellular and network mechanisms in the AC resulting in improved phase locked synchronization in developing *Fmr1* KO mice.

4.2 | Molecular mechanisms influencing *Fmr1* KO EEG phenotype

It is possible that changes in PV/PNN networks affect inhibitory circuits and neural oscillation patterns. The loss of PNNs is associated with abnormal plasticity and reduced excitability of PV interneurons (Balmer, 2016; Lensjo, Christensen, Tennoe, Fyhn, & Hafting, 2017; Chu et al., 2018). This may lead to altered balance of excitatory and inhibitory circuits, and improper network synchronization and hyperexcitability (Contractor, Klyachko, & Portera-Cailliau, 2015). In fact, several studies point altered functionality of GABAergic circuits, specifically fast-spiking PV interneurons in FXS (Goel et al., 2018; Nomura et al., 2017; Selby, Zhang, & Sun, 2007). Specifically, PV cell density is significantly reduced in the AC (Kulinich et al., 2019; Wen et al., 2018) and somatosensory cortex (Selby et al., 2007) of *Fmr1* KO mice compared to WT mice. One recent study demonstrated that passive developmental sound exposure during the maturation of synaptic and intrinsic properties (P9–21) results in enhanced PV cell density and PV/PNN co-localization in the AC of *Fmr1* KO mice despite impairment of PNN formation (Kulinich et al., 2019). In contrast, genetic reduction of MMP-9 was shown to enhance the formation of PNNs around PV cells in the AC (Wen et al., 2018). Our study shows that pharmacological inhibition of MMP-9 activity alone during the critical developmental period results in enhanced PNN formation around PV interneurons. While we did not see a significant increase in PV cell density, we did observe an increase in PV levels measured by Western blot, similar to what has been observed in other ASD models (Filice, Vorckel, Sungur, Wöhr, & Schwaller, 2016). It is possible that increased PNN formation around PV cells contributed to increased PV levels, which influenced the changes in resting state EEG oscillations in SB-3CT-treated *Fmr1* KO mice (Yamada, Ohgomori, & Jinno, 2015). To more effectively target auditory hypersensitivity, a combination of sensory stimulation (Kulinich et al., 2019; Woo & Leon, 2013) with pharmacological inhibition of MMP-9 activity (Bilousova et al., 2009) may yield a synergistic effect.

Other studies have employed sound exposure or mGluR5 inhibitors during the late postnatal window (P20–30) to rescue AC plasticity deficits and found that they were only able to rescue sound exposure-induced cortical map plasticity (size of A1 and response latency) when *Fmr1* KO mice were exposed to sound between P9–20 in conjunction with daily MPEP injections (Kim, Gibboni, Kirkhart, & Bao, 2013). It is possible that inhibition of MMP-9 activity may function as a potent therapeutic for auditory hypersensitivity and anxiety/hyperactivity phenotypes during the critical developmental period. The question remains whether administration of SB-3CT during the critical developmental period has more beneficial effects in regulating resting state EEG oscillations, improving responses to sound and anxiety/hyperactivity-related behaviors in *Fmr1* KO mice versus administration of SB-3CT in adult *Fmr1* KO mice. SB-3CT has only ~45 min half-life (Gooyit et al., 2012). However, even transient inhibition of MMP-9 activity during this specific developmental window was sufficient to trigger structural and functional changes in

the auditory cortex of *Fmr1* KO mice. One potential benefit may be attributed to the metabolism of SB-3CT, which functions as an irreversible inhibitor yielding covalent modifications that inhibit the activation of MMP-2/9 (Brown et al., 2000).

In addition to the enhanced PNN formation surrounding PV interneurons in the AC, the function of PV interneurons may also be influenced by activity of TrkB receptor. TrkB is shown to play a role in gamma-band synchronization in the hippocampal network (Zheng et al., 2011) and functions as a receptor for brain-derived neurotrophic factor (BDNF). In fact, TrkB is expressed by GABAergic neurons, in particular PV-positive cells (Cellerino, Maffei, & Domenici, 1996; Lewis et al., 2005). BDNF-mediated signaling is involved in mediating cell growth and survival, neuronal differentiation, and activity-dependent regulation of inhibitory synapse development (Hong, McCord, & Greenberg, 2008) and has been linked to maturation of PV cells in the cerebral cortex (Itami, Kimura, & Nakamura, 2007). BDNF via TrkB is known to promote the development of GABAergic neurons and induces the expression of GABA-related proteins, including GAD67, GAT1, and PV (Nomura et al., 2017; Xenos et al., 2018). Notably, BDNF-TrkB signaling has been shown to be impaired in *Fmr1* KO mice (Castren & Castren, 2014). We previously reported decreased phosphorylation of TrkB in the AC of *Fmr1* KO mice compared to WT mice, which was up-regulated following developmental exposure to sound (Kulinich et al., 2019). In the current study, we showed that treatment with SB-3CT increased TrkB phosphorylation in *Fmr1* KO mice compared to vehicle-treated *Fmr1* KO mice (Figure 7). Together, inhibition of MMP-9 activity may preferentially target PV-mediated inhibitory networks by influencing the stability of PV interneurons via increased PNN formation and activation of TrkB receptors.

4.3 | Inhibition of MMP-9 activity reduces AKT phosphorylation and improves anxiety and hyperactivity phenotypes in *Fmr1* KO mice

FXS is characterized by over-activation of group I metabotropic glutamate receptors (Huber, 2002), which promote Akt/mTOR signaling leading to aberrant phosphorylation of Akt and mTOR-related proteins, and increased protein synthesis (Bear, Huber, & Warren, 2004; Sharma et al., 2010). Studies have shown that genetic reduction of p70 ribosomal S6 kinase 1 (S6K1) prevented elevated phosphorylation of translational control proteins, normalizing protein synthesis, reversing dendritic spine deficits, and improving social interactions, novel object recognition, and behavioral flexibility in *Fmr1* KO mice (Bhattacharya et al., 2012). In fact, several studies link dysregulation of mTOR signaling with dendritic and synaptic abnormalities, cognitive impairments, and behavioral performance in FXS (Bhattacharya et al., 2012; Busquets-Garcia, Maldonado, & Ozaita, 2014; Troca-Marin, Alves-Sampaio, & Montesinos, 2012). Furthermore, treatment with the antibiotic minocycline, which is known to inhibit MMP-9, also promotes dendritic spine maturation and improves behavioral performance in developing *Fmr1* KO mice



(Bilousova et al., 2009). Thus, it is possible that the reduction of Akt phosphorylation observed in *Fmr1* KO mice following treatment with SB-3CT may be linked to the changes in dendritic and synaptic profiles affecting protein synthesis, synaptic plasticity, and behavioral performance.

While *Fmr1* KO mice display multiple behavioral impairments that parallel human patients with FXS (Bernardet & Crusio, 2006), there is wide variability in behavioral results assessing anxiety, hyperactivity, social, and cognitive impairments in *Fmr1* KO mice. Several studies find these measures to be altered (Bilousova et al., 2009; Ding, Sethna, & Wang, 2014; Sinclair et al., 2017), while others show no differences (Kazdoba, Leach, Silverman, & Crawley, 2014). We show that vehicle-treated *Fmr1* KO mice spent less time in the open arms of the EPM, similar to previous studies in our laboratory (Bilousova et al., 2009), as well as increased percent time in thigmotaxis and decreased center entries in the OF, indicating higher anxiety. *Fmr1* KO mice also displayed increased hyperactivity indicated by increased speed in both EPM and OF tests. Interestingly, treatment with SB-3CT reduced both anxiety and hyperactivity measures in *Fmr1* KO mice. These results suggest that SB-3CT effectively ameliorates behavioral impairments observed in developing *Fmr1* KO mice when MMP-9 activity is inhibited during the specific developmental period.

In conclusion, we have shown that acute inhibition of MMP-9 activity during a specific critical developmental period (P22–P28) may serve to modulate PV neuron-mediated inhibitory circuits, neural oscillatory patterns, and behavioral impairments associated with FXS. These findings implicate MMP-9 as a potent candidate contributing to the FXS phenotype and indicate that targeted inhibition of MMP-9 activity may be a promising therapeutic agent.

ACKNOWLEDGEMENTS

Supported by National Institute of Mental Health, National Institute of Child Health and Human Development U54 HD082008-01. FRAXA Research Foundation Postdoctoral Fellowship to P.S.P and J.W.L and a University of California President's Postdoctoral Fellowship to P.S.P. Thank you to the Ethell, Binder, and Razak laboratories. A special thank you to all who contributed to the current research including Teresa H. Wen for training with surgeries, Carrie R. Jonak for assistance in mouse colony maintenance, Anna Kulinich for assistance in creating graphics and illustrations, and Dushan Rakic, Yasmien Hanania, Mark Makar, and Rashid Syed for technical assistance.

All experiments were conducted in compliance with the ARRIVE guidelines.

CONFLICT OF INTEREST

The authors declare no competing financial interests.

ORCID

Patricia S. Pirbhoy  <https://orcid.org/0000-0001-8733-7447>

Jonathan W. Lovelace  <https://orcid.org/0000-0001-5734-6801>

Iryna M. Ethell  <https://orcid.org/0000-0002-1324-6611>

REFERENCES

- Anderson, L. A., Christianson, G. B., & Linden, J. F. (2009). Mouse auditory cortex differs from visual and somatosensory cortices in the laminar distribution of cytochrome oxidase and acetylcholinesterase. *Brain Research*, 1252, 130–142. <https://doi.org/10.1016/j.brainres.2008.11.037>
- Artieda, J., Valencia, M., Alegre, M., Olaziregi, O., Urrestarazu, E., & Iriarte, J. (2004). Potentials evoked by chirp-modulated tones: A new technique to evaluate oscillatory activity in the auditory pathway. *Clinical Neurophysiology*, 115, 699–709. <https://doi.org/10.1016/j.clinph.2003.10.021>
- Balakrishnan, S., & Pearce, R. A. (2014). Spatiotemporal characteristics and pharmacological modulation of multiple gamma oscillations in the CA1 region of the hippocampus. *Frontiers in Neural Circuits*, 8, 150.
- Balmer, T. S. (2016). Perineuronal nets enhance the excitability of fast-spiking neurons. *Eneuro*, 3(4), 1–13.
- Barry, R. J., Clarke, A. R., Johnstone, S. J., McCarthy, R., & Selikowitz, M. (2009). Electroencephalogram theta/beta ratio and arousal in attention-deficit/hyperactivity disorder: Evidence of independent processes. *Biological Psychiatry*, 66, 398–401.
- Barry, R. J., Johnstone, S. J., & Clarke, A. R. (2003). A review of electrophysiology in attention-deficit/hyperactivity disorder: II. Event-related Potentials. *Clin Neurophysiol*, 114, 184–198. [https://doi.org/10.1016/S1388-2457\(02\)00363-2](https://doi.org/10.1016/S1388-2457(02)00363-2)
- Bear, M. F., Huber, K. M., & Warren, S. T. (2004). The mGluR theory of fragile X mental retardation. *Trends in Neurosciences*, 27, 370–377. <https://doi.org/10.1016/j.tins.2004.04.009>
- Bernardet, M., & Crusio, W. E. (2006). *Fmr1* KO mice as a possible model of autistic features. *ScientificWorldJournal*, 6, 1164–1176.
- Bhattacharya, A., Kaphzan, H., Alvarez-Dieppa, A. C., Murphy, J. P., Pierre, P., & Klann, E. (2012). Genetic removal of p70 S6 kinase 1 corrects molecular, synaptic, and behavioral phenotypes in fragile X syndrome mice. *Neuron*, 76, 325–337. <https://doi.org/10.1016/j.neuron.2012.07.022>
- Bilousova, T. V., Dansie, L., Ngo, M., Aye, J., Charles, J. R., Ethell, D. W., & Ethell, I. M. (2009). Minocycline promotes dendritic spine maturation and improves behavioural performance in the fragile X mouse model. *Journal of Medical Genetics*, 46, 94–102. <https://doi.org/10.1136/jmg.2008.061796>
- Born, H. A., Dao, A. T., Levine, A. T., Lee, W. L., Mehta, N. M., Mehra, S., ... Anderson, A. E. (2017). Strain-dependence of the Angelman Syndrome phenotypes in Ube3a maternal deficiency mice. *Scientific Reports*, 7, 8451. <https://doi.org/10.1038/s41598-017-08825-x>
- Brown, S., Bernardo, M. M., Li, Z. H., Kotra, L. P., Tanaka, Y., Fridman, R., & Mobashery, S. (2000). Potent and selective mechanism-based inhibition of gelatinases. *Journal of the American Chemical Society*, 122, 6799–6800. <https://doi.org/10.1021/ja001461n>
- Busquets-Garcia, A., Maldonado, R., & Ozaita, A. (2014). New insights into the molecular pathophysiology of fragile X syndrome and therapeutic perspectives from the animal model. *International Journal of Biochemistry & Cell Biology*, 53, 121–126. <https://doi.org/10.1016/j.biocel.2014.05.004>
- Buzsaki, G., & Wang, X. J. (2012). Mechanisms of gamma oscillations. *Annual Review of Neuroscience*, 35, 203–225. <https://doi.org/10.1146/annurev-neuro-062111-150444>
- Castren, M. L., & Castren, E. (2014). BDNF in fragile X syndrome. *Neuropharmacology*, 76, 729–736.
- Castren, M., Paakkonen, A., Tarkka, I. M., Ryyanen, M., & Partanen, J. (2003). Augmentation of auditory N1 in children with fragile X syndrome. *Brain Topography*, 15, 165–171.
- Cellerino, A., Maffei, L., & Domenici, L. (1996). The distribution of brain-derived neurotrophic factor and its receptor trkB in parvalbumin-containing neurons of the rat visual cortex. *European Journal of Neuroscience*, 8, 1190–1197.

- Chu, P., Abraham, R., Budhu, K., Khan, U., De Marco Garcia, N., & Brumberg, J. C. (2018). The impact of perineuronal net digestion using chondroitinase ABC on the intrinsic physiology of cortical neurons. *Neuroscience*, 388, 23–35. <https://doi.org/10.1016/j.neuroscience.2018.07.004>
- Contractor, A., Klyachko, V. A., & Portera-Cailliau, C. (2015). Altered neuronal and circuit excitability in fragile X syndrome. *Neuron*, 87, 699–715. <https://doi.org/10.1016/j.neuron.2015.06.017>
- Crane, L., Goddard, L., & Pring, L. (2009). Sensory processing in adults with autism spectrum disorders. *Autism*, 13, 215–228. <https://doi.org/10.1177/1362361309103794>
- Crawford, D. C., Acuna, J. M., & Sherman, S. L. (2001). FMR1 and the fragile X syndrome: Human genome epidemiology review. *Genetics in Medicine*, 3, 359–371. <https://doi.org/10.1097/00125817-200109000-00006>
- Dansie, L. E., Phommahaxay, K., Okusanya, A. G., Uwadia, J., Huang, M., Rotschafer, S. E., ... Ethell, I. M. (2013). Long-lasting effects of minocycline on behavior in young but not adult Fragile X mice. *Neuroscience*, 246, 186–198. <https://doi.org/10.1016/j.neuroscience.2013.04.058>
- Ding, Q., Sethna, F., & Wang, H. (2014). Behavioral analysis of male and female Fmr1 knockout mice on C57BL/6 background. *Behavioral Brain Research*, 271, 72–78. <https://doi.org/10.1016/j.bbr.2014.05.046>
- Dvorak, D., & Fenton, A. A. (2014). On track with two gammas. *Neuron*, 82, 506–508. <https://doi.org/10.1016/j.neuron.2014.04.027>
- Dziembowska, M., Pretto, D. I., Janusz, A., Kaczmarek, L., Leigh, M. J., Gabriel, N., ... Tassone, F. (2013). High MMP-9 activity levels in fragile X syndrome are lowered by minocycline. *American Journal of Medical Genetics. Part A*, 161A, 1897–1903. <https://doi.org/10.1002/ajmg.a.36023>
- Ethridge, L. E., De Stefano, L. A., Schmitt, L. M., Woodruff, N. E., Brown, K. L., Tran, M., ... Sweeney, J. A. (2019). Auditory EEG biomarkers in fragile X syndrome: Clinical relevance. *Front Integr Neurosci*, 13, 60. <https://doi.org/10.3389/fnint.2019.00060>
- Ethridge, L. E., White, S. P., Mosconi, M. W., Wang, J., Byerly, M. J., & Sweeney, J. A. (2016). Reduced habituation of auditory evoked potentials indicate cortical hyper-excitability in Fragile X Syndrome. *Transl Psychiatry*, 6, e787. <https://doi.org/10.1038/tp.2016.48>
- Ethridge, L. E., White, S. P., Mosconi, M. W., Wang, J., Pedapati, E. V., Erickson, C. A., ... Sweeney, J. A. (2017). Neural synchronization deficits linked to cortical hyper-excitability and auditory hypersensitivity in fragile X syndrome. *Molecular Autism*, 8, 22. <https://doi.org/10.1186/s13229-017-0140-1>
- Filice, F., Vorckel, K. J., Sungur, A. O., Wohr, M., & Schwaller, B. (2016). Reduction in parvalbumin expression not loss of the parvalbumin-expressing GABA interneuron subpopulation in genetic parvalbumin and shank mouse models of autism. *Molecular Brain*, 9, 10. <https://doi.org/10.1186/s13041-016-0192-8>
- Gibson, J. R., Bartley, A. F., Hays, S. A., & Huber, K. M. (2008). Imbalance of neocortical excitation and inhibition and altered UP states reflect network hyperexcitability in the mouse model of fragile X syndrome. *Journal of Neurophysiology*, 100, 2615–2626. <https://doi.org/10.1152/jn.90752.2008>
- Gkogkas, C. G., Khoutorsky, A., Cao, R., Jafarnejad, S. M., Prager-Khoutorsky, M., Giannakas, N., ... Sonenberg, N. (2014). Pharmacogenetic inhibition of eIF4E-dependent Mmp9 mRNA translation reverses fragile X syndrome-like phenotypes. *Cell Reports*, 9, 1742–1755. <https://doi.org/10.1016/j.celrep.2014.10.064>
- Goel, A., Cantu, D. A., Guilfoyle, J., Chaudhari, G. R., Newadkar, A., Todisco, B., ... Portera-Cailliau, C. (2018). Impaired perceptual learning in a mouse model of Fragile X syndrome is mediated by parvalbumin neuron dysfunction and is reversible. *Nature Neuroscience*, 21, 1404–1411. <https://doi.org/10.1038/s41593-018-0231-0>
- Gooyit, M., Suckow, M. A., Schroeder, V. A., Wolter, W. R., Mobashery, S., & Chang, M. (2012). Selective gelatinase inhibitor neuroprotective agents cross the blood-brain barrier. *ACS Chemical Neuroscience*, 3, 730–736. <https://doi.org/10.1021/cn300062w>
- Hagerman, R. J., Rivera, S. M., & Hagerman, P. J. (2008). The fragile X family of disorders: A model for autism and targeted treatments. *Current Pediatric Reviews*, 4, 40–52.
- Hong, E. J., McCord, A. E., & Greenberg, M. E. (2008). A biological function for the neuronal activity-dependent component of Bdnf transcription in the development of cortical inhibition. *Neuron*, 60, 610–624. <https://doi.org/10.1016/j.neuron.2008.09.024>
- Huber, K. M., Gallagher, S. M., Warren, S. T., & Bear, M. F. (2002). Altered synaptic plasticity in a mouse model of fragile X mental retardation. *Proceedings of the National Academy of Sciences*, 99, 7746–7750. <https://doi.org/10.1073/pnas.122205699>
- Itami, C., Kimura, F., & Nakamura, S. (2007). Brain-derived neurotrophic factor regulates the maturation of layer 4 fast-spiking cells after the second postnatal week in the developing barrel cortex. *Journal of Neuroscience*, 27, 2241–2252. <https://doi.org/10.1523/JNEUROSCI.3345-06.2007>
- Jensen, O., & Mazaheri, A. (2010). Shaping functional architecture by oscillatory alpha activity: Gating by inhibition. *Frontiers in Human Neuroscience*, 4, 186. <https://doi.org/10.3389/fnhum.2010.00186>
- Kaufmann, W. E., Cortell, R., Kau, A. S., Bukelis, I., Tierney, E., Gray, R. M., ... Stanard, P. (2004). Autism spectrum disorder in fragile X syndrome: Communication, social interaction, and specific behaviors. *American Journal of Medical Genetics. Part A*, 129A, 225–234. <https://doi.org/10.1002/ajmg.a.30229>
- Kazdoba, T. M., Leach, P. T., Silverman, J. L., & Crawley, J. N. (2014). Modeling fragile X syndrome in the Fmr1 knockout mouse. *Intractable & Rare Diseases Research*, 3, 118–133.
- Kim, H., Gibboni, R., Kirkhart, C., & Bao, S. (2013). Impaired critical period plasticity in primary auditory cortex of fragile X model mice. *Journal of Neuroscience*, 33, 15686–15692. <https://doi.org/10.1523/JNEUROSCI.3246-12.2013>
- Klann, E., & Dever, T. E. (2004). Biochemical mechanisms for translational regulation in synaptic plasticity. *Nature Reviews. Neuroscience*, 5, 931–942.
- Klimesch, W. (1999). EEG alpha and theta oscillations reflect cognitive and memory performance: A review and analysis. *Brain Research. Brain Research Reviews*, 29, 169–195. [https://doi.org/10.1016/S0165-0173\(98\)00056-3](https://doi.org/10.1016/S0165-0173(98)00056-3)
- Kulinich, A. O., Reinhard, S. M., Rais, M., Lovelace, J. W., Scott, V., Binder, D. K., ... Ethell, I. M. (2019). Beneficial effects of sound exposure on auditory cortex development in a mouse model of Fragile X Syndrome. *Neurobiology of Diseases*, 134, 104622. <https://doi.org/10.1016/j.nbd.2019.104622>
- Lagerbauer, B. (2001). Evidence that fragile X mental retardation protein is a negative regulator of translation. *Human Molecular Genetics*, 10, 329–338. <https://doi.org/10.1093/hmg/10.4.329>
- Lenzjo, K. K., Christensen, A. C., Tennoe, S., Fyhn, M., & Hafting, T. (2017). Differential expression and cell-type specificity of perineuronal nets in hippocampus, medial entorhinal cortex, and visual cortex examined in the rat and mouse. *eNeuro*, 4(3), 1–18.
- Lewis, D. A., Hashimoto, T., & Volk, D. W. (2005). Cortical inhibitory neurons and schizophrenia. *Nature Reviews. Neuroscience*, 6, 312–324.
- Lovelace, J. W., Ethell, I. M., Binder, D. K., & Razak, K. A. (2018). Translation-relevant EEG phenotypes in a mouse model of Fragile X Syndrome. *Neurobiology of Diseases*, 115, 39–48. <https://doi.org/10.1016/j.nbd.2018.03.012>
- Lovelace, J. W., Rais, M., Palacios, A. R., Shuai, X. S., Bishay, S., Popa, O., ... Razak, K. A. (2019). Deletion of Fmr1 from forebrain excitatory neurons triggers abnormal cellular, EEG, and behavioral phenotypes in the auditory cortex of a mouse model of fragile X syndrome. *Cerebral Cortex*, 30(3), 969–988. <https://doi.org/10.1093/cercor/bhz141>
- Lovelace, J. W., Wen, T. H., Reinhard, S., Hsu, M. S., Sidhu, H., Ethell, I. M., ... Razak, K. A. (2016). Matrix metalloproteinase-9 deletion rescues

- auditory evoked potential habituation deficit in a mouse model of Fragile X Syndrome. *Neurobiology of Diseases*, 89, 126–135. <https://doi.org/10.1016/j.nbd.2016.02.002>
- Maris, E., & Oostenveld, R. (2007). Nonparametric statistical testing of EEG- and MEG-data. *Journal of Neuroscience Methods*, 164, 177–190. <https://doi.org/10.1016/j.jneumeth.2007.03.024>
- Martin del Campo, H. N., Measor, K. R., & Razak, K. A. (2012). Parvalbumin immunoreactivity in the auditory cortex of a mouse model of presbycusis. *Hearing Research*, 294, 31–39. <https://doi.org/10.1016/j.heares.2012.08.017>
- Mathewson, K. E., Lleras, A., Beck, D. M., Fabiani, M., Ro, T., & Gratton, G. (2011). Pulsed out of awareness: EEG alpha oscillations represent a pulsed-inhibition of ongoing cortical processing. *Frontiers in Psychology*, 2, 99. <https://doi.org/10.3389/fpsyg.2011.00099>
- McDiarmid, T. A., Bernardos, A. C., & Rankin, C. H. (2017). Habituation is altered in neuropsychiatric disorders—a comprehensive review with recommendations for experimental design and analysis. *Neuroscience and Biobehavioral Reviews*, 80, 286–305. <https://doi.org/10.1016/j.neubiorev.2017.05.028>
- Miller, L. J., McIntosh, D. N., McGrath, J., Shyu, V., Lampe, M., Taylor, A. K., ... Hagerman, R. J. (1999). Electrodermal responses to sensory stimuli in individuals with fragile X syndrome: A preliminary report. *American Journal of Medical Genetics*, 83, 268–279. [https://doi.org/10.1002/\(SICI\)1096-8628\(19990402\)83:4<268:AID-AJMG7>3.0.CO;2-K](https://doi.org/10.1002/(SICI)1096-8628(19990402)83:4<268:AID-AJMG7>3.0.CO;2-K)
- Niell, C. M., & Stryker, M. P. (2010). Modulation of visual responses by behavioral state in mouse visual cortex. *Neuron*, 65, 472–479. <https://doi.org/10.1016/j.neuron.2010.01.033>
- Nomura, T., Musial, T. F., Marshall, J. J., Zhu, Y., Remmers, C. L., Xu, J., ... Contractor, A. (2017). Delayed maturation of fast-spiking interneurons is rectified by activation of the TrkB receptor in the mouse model of fragile X syndrome. *Journal of Neuroscience*, 37, 11298–11310. <https://doi.org/10.1523/JNEUROSCI.2893-16.2017>
- Oswald, A. M., & Reyes, A. D. (2008). Maturation of intrinsic and synaptic properties of layer 2/3 pyramidal neurons in mouse auditory cortex. *Journal of Neurophysiology*, 99, 2998–3008. <https://doi.org/10.1152/jn.01160.2007>
- Paluszkiwicz, S. M., Olmos-Serrano, J. L., Corbin, J. G., & Huntsman, M. M. (2011). Impaired inhibitory control of cortical synchronization in fragile X syndrome. *Journal of Neurophysiology*, 106, 2264–2272. <https://doi.org/10.1152/jn.00421.2011>
- Perez-Alcazar, M., Nicolas, M. J., Valencia, M., Alegre, M., Iriarte, J., & Artieda, J. (2008). Chirp-evoked potentials in the awake and anesthetized rat. A procedure to assess changes in cortical oscillatory activity. *Experimental Neurology*, 210, 144–153. <https://doi.org/10.1016/j.expneurol.2007.10.017>
- Purcell, D. W., John, S. M., Schneider, B. A., & Picton, T. W. (2004). Human temporal auditory acuity as assessed by envelope following responses. *Journal of the Acoustical Society of America*, 116, 3581–3593. <https://doi.org/10.1121/1.1798354>
- Radwan, B., Dvorak, D., & Fenton, A. A. (2016). Impaired cognitive discrimination and discoordination of coupled theta-gamma oscillations in Fmr1 knockout mice. *Neurobiology of Diseases*, 88, 125–138. <https://doi.org/10.1016/j.nbd.2016.01.003>
- Rais, M., Binder, D. K., Razak, K. A., & Ethell, I. M. (2018). Sensory processing phenotypes in fragile X syndrome. *ASN Neuro*, 10, 1759091418801092. <https://doi.org/10.1177/1759091418801092>
- Ray, S., & Maunsell, J. H. (2011). Different origins of gamma rhythm and high-gamma activity in macaque visual cortex. *PLoS Biology*, 9, e1000610. <https://doi.org/10.1371/journal.pbio.1000610>
- Rotschafer, S., & Razak, K. (2013). Altered auditory processing in a mouse model of fragile X syndrome. *Brain Research*, 1506, 12–24. <https://doi.org/10.1016/j.brainres.2013.02.038>
- Schneider, A., Leigh, M. J., Adams, P., Nanakul, R., Chechi, T., Olichney, J., ... Hessler, D. (2013). Electro-cortical changes associated with minocycline treatment in fragile X syndrome. *J Psychopharmacol*, 27, 956–963. <https://doi.org/10.1177/0269881113494105>
- Selby, L., Zhang, C., & Sun, Q. Q. (2007). Major defects in neocortical GABAergic inhibitory circuits in mice lacking the fragile X mental retardation protein. *Neuroscience Letters*, 412, 227–232. <https://doi.org/10.1016/j.neulet.2006.11.062>
- Sharma, A., Hoeffler, C. A., Takayasu, Y., Miyawaki, T., McBride, S. M., Klann, E., & Zukin, R. S. (2010). Dysregulation of mTOR signaling in fragile X syndrome. *Journal of Neuroscience*, 30, 694–702. <https://doi.org/10.1523/JNEUROSCI.3696-09.2010>
- Sidhu, H., Dansie, L. E., Hickmott, P. W., Ethell, D. W., & Ethell, I. M. (2014). Genetic removal of matrix metalloproteinase 9 rescues the symptoms of fragile X syndrome in a mouse model. *Journal of Neuroscience*, 34, 9867–9879. <https://doi.org/10.1523/JNEUROSCI.1162-14.2014>
- Siller, S. S., & Broadie, K. (2011). Neural circuit architecture defects in a Drosophila model of Fragile X syndrome are alleviated by minocycline treatment and genetic removal of matrix metalloproteinase. *Disease Models & Mechanisms*, 4, 673–685. <https://doi.org/10.1242/dmm.008045>
- Sinclair, D., Oranje, B., Razak, K. A., Siegel, S. J., & Schmid, S. (2017). Sensory processing in autism spectrum disorders and Fragile X syndrome—From the clinic to animal models. *Neuroscience and Biobehavioral Reviews*, 76, 235–253. <https://doi.org/10.1016/j.neubiorev.2016.05.029>
- Sohal, V. S., Zhang, F., Yizhar, O., & Deisseroth, K. (2009). Parvalbumin neurons and gamma rhythms enhance cortical circuit performance. *Nature*, 459, 698–702. <https://doi.org/10.1038/nature07991>
- Talisa, V. B., Boyle, L., Crafa, D., & Kaufmann, W. E. (2014). Autism and anxiety in males with fragile X syndrome: An exploratory analysis of neurobehavioral profiles from a parent survey. *American Journal of Medical Genetics. Part A*, 164A, 1198–1203. <https://doi.org/10.1002/ajmg.a.36468>
- Tallon-Baudry, C., Bertrand, O., Delpuech, C., & Pernier, J. (1996). Stimulus specificity of phase-locked and non-phase-locked 40 Hz visual responses in human. *Journal of Neuroscience*, 16, 4240–4249.
- Toledo, M. A., Wen, T. H., Binder, D. K., Ethell, I. M., & Razak, K. A. (2019). Reversal of ultrasonic vocalization deficits in a mouse model of Fragile X Syndrome with minocycline treatment or genetic reduction of MMP-9. *Behavioral Brain Research*, 372, 112068. <https://doi.org/10.1016/j.bbr.2019.112068>
- Troca-Marin, J. A., Alves-Sampaio, A., & Montesinos, M. L. (2012). Deregulated mTOR-mediated translation in intellectual disability. *Progress in Neurobiology*, 96, 268–282. <https://doi.org/10.1016/j.pneurobio.2012.01.005>
- Van der Molen, M. J., & Van der Molen, M. W. (2013). Reduced alpha and exaggerated theta power during the resting-state EEG in fragile X syndrome. *Biological Psychology*, 92, 216–219. <https://doi.org/10.1016/j.biopsycho.2012.11.013>
- Vandooren, J., Geurts, N., Martens, E., Van den Steen, P. E., Jonghe, S. D., Herdewijn, P., & Opendakker, G. (2011). Gelatin degradation assay reveals MMP-9 inhibitors and function of O-glycosylated domain. *World Journal of Biological Chemistry*, 2, 14–24. <https://doi.org/10.4331/wjbc.v2.i1.14>
- Verkerk, A. J. M. H., Pieretti, M., Sutcliffe, J. S., Fu, Y.-H., Kuhl, D. P. A., Pizzuti, A., ... Warren, S. T. (1991). Identification of a gene (FMR-1) containing a CGG repeat coincident with a breakpoint cluster region exhibiting length variation in fragile X syndrome. *Cell*, 65, 905–914. [https://doi.org/10.1016/0092-8674\(91\)90397-H](https://doi.org/10.1016/0092-8674(91)90397-H)
- Vreugdenhil, M., Jefferys, J. G., Celio, M. R., & Schwaller, B. (2003). Parvalbumin-deficiency facilitates repetitive IPSCs and gamma oscillations in the hippocampus. *Journal of Neurophysiology*, 89, 1414–1422. <https://doi.org/10.1152/jn.00576.2002>
- Wang, J., Barstein, J., Ethridge, L. E., Mosconi, M. W., Takarae, Y., & Sweeney, J. A. (2013). Resting state EEG abnormalities in autism spectrum disorders. *Journal of Neurodevelopmental Disorders*, 5, 24. <https://doi.org/10.1186/1866-1955-5-24>



- Wang, J., Ethridge, L. E., Mosconi, M. W., White, S. P., Binder, D. K., Pedapati, E. V., ... Sweeney, J. A. (2017). A resting EEG study of neocortical hyperexcitability and altered functional connectivity in fragile X syndrome. *Journal of Neurodevelopmental Disorders*, 9, 11. <https://doi.org/10.1186/s11689-017-9191-z>
- Wen, T. H., Afroz, S., Reinhard, S. M., Palacios, A. R., Tapia, K., Binder, D. K., ... Ethell, I. M. (2018). Genetic reduction of matrix metalloproteinase-9 promotes formation of perineuronal nets around parvalbumin-expressing interneurons and normalizes auditory cortex responses in developing *Fmr1* knock-out mice. *Cerebral Cortex*, 28, 3951–3964. <https://doi.org/10.1093/cercor/bhx258>
- Wen, T. H., Lovelace, J. W., Ethell, I. M., Binder, D. K., & Razak, K. A. (2019). Developmental Changes in EEG Phenotypes in a Mouse Model of Fragile X Syndrome. *Neuroscience*, 398, 126–143. <https://doi.org/10.1016/j.neuroscience.2018.11.047>
- Woo, C. C., & Leon, M. (2013). Environmental enrichment as an effective treatment for autism: A randomized controlled trial. *Behavioral Neuroscience*, 127, 487–497. <https://doi.org/10.1037/a0033010>
- Xenos, D., Kamceva, M., Tomasi, S., Cardin, J. A., Schwartz, M. L., & Vaccarino, F. M. (2018). Loss of TrkB signaling in parvalbumin-expressing basket cells results in network activity disruption and abnormal behavior. *Cerebral Cortex*, 28, 3399–3413. <https://doi.org/10.1093/cercor/bhx173>
- Yamada, J., Ohgomori, T., & Jinno, S. (2015). Perineuronal nets affect parvalbumin expression in GABAergic neurons of the mouse hippocampus. *European Journal of Neuroscience*, 41, 368–378. <https://doi.org/10.1111/ejn.12792>
- Yan, Q. J., Asafo-Adjei, P. K., Arnold, H. M., Brown, R. E., & Bauchwitz, R. P. (2004). A phenotypic and molecular characterization of the *fmr1*-tm1Cgr fragile X mouse. *Genes, Brain, and Behavior*, 3, 337–359. <https://doi.org/10.1111/j.1601-183X.2004.00087.x>
- Yan, Q. J., Rammal, M., Tranfaglia, M., & Bauchwitz, R. P. (2005). Suppression of two major Fragile X Syndrome mouse model phenotypes by the mGluR5 antagonist MPEP. *Neuropharmacology*, 49, 1053–1066. <https://doi.org/10.1016/j.neuropharm.2005.06.004>
- Zheng, K., An, J. J., Yang, F., Xu, W., Xu, Z.-q D., Wu, J., ... Lu, B. (2011). TrkB signaling in parvalbumin-positive interneurons is critical for gamma-band network synchronization in hippocampus. *Proceedings of the National Academy of Sciences*, 108, 17201–17206. <https://doi.org/10.1073/pnas.1114241108>

SUPPORTING INFORMATION

Additional supporting information may be found online in the Supporting Information section.

How to cite this article: PIRBHOYPS, Rais M, Lovelace JW, et al. Acute pharmacological inhibition of matrix metalloproteinase-9 activity during development restores perineuronal net formation and normalizes auditory processing in *Fmr1* KO mice. *J. Neurochem.* 2020;00:1–21. <https://doi.org/10.1111/jnc.15037>